SOPHIA: A mineralogical simulant for phyllosilicate terrains at the *Rosalind Franklin* landing site, Oxia Planum, Mars.

A. Dugdale[1*], N.K. Ramkissoon[2], P. Fawdon[3] M.R. Patel[1], L. Hills[3], G. Degli-Alessandrini[3], E. Bonsall[4], C. Schröder[4], S.M.R. Turner[2], C.N. Achilles[5], V.K. Pearson[1].

[1]AstrobiologyOU, School of Physical Sciences, The Open University, Walton Hall, Milton Keynes, United Kingdom, MK7 6AA

[2]AstrobiologyOU, School of Environment Earth and Ecosystem Sciences, The Open University, Walton Hall, Milton Keynes, United Kingdom, MK7 6AA

[3]School of Physical Sciences, The Open University, Walton Hall, Milton Keynes, United Kingdom, MK7 6AA

[4]Biological and Environmental Sciences, Faculty of Natural Sciences, University of Stirling, Stirling FK9 4LA, UK

[5]NASA Goddard Space Flight Center, Greenbelt, MD, USA/ Center for Research and Exploration in Space Science and Technology, University of Maryland, College Park, MD, USA

*Corresponding author (email address: amy.dugdale@open.ac.uk)

Abstract

The phyllosilicate-bearing martian plain, Oxia Planum, is the proposed landing site for the *Rosalind Franklin* rover mission, scheduled to launch in 2028. *Rosalind Franklin* which will search for signs of past or present life on Mars. Terrestrial analogue sites and simulants can be used to test instruments analogous to those on *Rosalind Franklin*, however no simulant for Oxia Planum currently exists. In anticipation of *this mission*, a simulant - SOPHIA (Simulant for Oxia Planum: Hydrated, Igneous, and Amorphous) - representative of the local mineralogy at Oxia Planum has been developed for biosignature and mineralogy experiments, which will assist in interpreting data returned by the rover. The simulant is derived from orbital observations of Oxia Planum and its catchment area. As no *in situ* data is available for Oxia Planum, mineralogy from other comparable sites on Mars was used to design the simulant including orbital data from Arabia Terra and Mawrth Vallis and *in situ* data collected from Gale crater. The mineralogy, chemistry and physical properties of the simulant were characterised

using standard laboratory techniques (SEM-EDS, XRF, XRD).Techniques analogous to rover instruments (Raman spectroscopy, Near-IR spectroscopy analogous to the Raman laser spectrometer and ISEM and MicrOmega instruments) were also used. The simulant is rich in Fe/Mg phyllosilicates with additional primary igneous and other alteration minerals and is an appropriate spectral and mineralogical analogue for Oxia Planum.

Keywords

Mineralogy, Mars, Surface, Regolith, Astrobiology.

1 Introduction

Oxia Planum is the landing site for the European Space Agency's Mars rover, *Rosalind Franklin*. The rover will search for evidence of past or present life and characterise the geochemical environment on the surface and in the near subsurface (Vago et al. 2017). *Rosalind Franklin* is designed to identify both physical biosignatures, such as microfossils (García-Ruiz *et al.* 2003; Schopf *et al.* 2012) and microbially-induced sedimentary structures (Noffke *et al.* 2001, 2013) and chemical biosignatures, including biominerals, isotopes and organic molecules (biomarkers), that are indicative of processes unique to life (Bazylinski and Moskowitz 1997; Beard *et al.* 1999; Banfield *et al.* 2001; Simoneit 2004; Georgiou and Deamer 2014; Moreras-Marti *et al.* 2022). To identify biomarkers, the rover will use a specifically-selected suite of instruments including the Mars Organic Molecule Analyser (MOMA) which includes Gas Chromatography-Mass and Laser Desorption-Mass Spectrometry (GCMS and LDMS; Goesmann *et al.* 2017) and the Raman Laser Spectrometer (RLS; Rull *et al.* 2017) .To Study the mineralogy of the site, RLS will be used in conjunction with the Infrared spectrometer for ExoMars (ISEM; Korablev *et al.* 2017), a visible near-infrared hyperspectral microscope (MicrOmega; Bibring *et al.* 2017)), the Mars Multispectral Imager for Subsurface Studies (Ma_MISS; De Sanctis *et al.* 2017, 2022), multispectral Panoramic cameras with geologically specific filters (PanCam; Cousins *et al.* 2012; Harris *et al.* 2015; Coates *et al.* 2017) and the CLose-UP Imager (CLUPI; Josset *et al.* 2017).

Despite the application of this instrument suite, biomarkers may remain undetected or unrecognised because they can be degraded or modified over geological time by processes such as UV and cosmic radiation (Kminek and Bada 2006; Dartnell *et al.* 2007, 2012), burial, diagenesis (Tan and Sephton 2020) and impacts (Parnell *et al.* 2005; Bowden *et al.* 2009; Montgomery *et al.* 2016). For example, variance in the shock impendence of minerals has been shown to create microscale pressure and temperature environments that may degrade biomarkers to variable degrees; degradation of amino acids has been shown to be higher in a haematite host mineralogy than in olivine (Furukawa *et al.* 2018). Local mineralogy can also control the detectability of organic species. For example, highly

absorbent or oxidising minerals can make the extraction and detection of biomarkers difficult (Röling *et al.* 2015) and the presence of perchlorates on the martian surface (Hecht *et al.* 2009; Glavin *et al.* 2013; Clark *et al.* 2021) has been proposed to modify organic species during the py-GC-MS experiments on the Curiosity rover (Millan *et al.* 2020); perchlorates can become highly oxidizing and may destroy or transform biomarkers into chlorinated species (Steininger *et al.* 2012; He *et al.* 2020). Thus, the mineral matrix which hosts biomarkers is important for understanding their preservation and detectability.

Mineralogy can also play a role in the preservation and longevity of biomarkers. Importantly, phyllosilicate minerals have been shown to adsorb organic molecules into the layered structure (Hedges 1977), protecting them from degradation by radiation and oxidation (Poch *et al.* 2015; dos Santos *et al.* 2016; Ertem *et al.* 2017). Phyllosilicates have also been shown to preserve amino acids from degradation by UV radiation (dos Santos *et al.* 2016). Phyllosilicates have been detected from orbit at Oxia Planum by the Observatoire pour la Minéralogie, l'Eau, les Glaces et l'Activité (OMEGA; Bibring *et al.* 2005) and Compact Reconnaissance Imaging Spectrometer for Mars (CRISM; Murchie et al., 2007) (i.e., Carter et al., 2016; Mandon et al., 2016; Brossier et al., 2022), providing evidence of aqueous activity within the region that could indicate it was once habitable (Carter *et al.* 2016; Vago *et al.* 2017). This terrain is the primary target of the *Rosalind Franklin* mission because of this organic preservation potential (Parnell *et al.* 2007; Fraser *et al.* 2011; Poch *et al.* 2015; Broz 2020).

In anticipation of landing at Oxia Planum, and in the absence of direct samples or analyses of this region of Mars, terrestrial analogues and simulants are essential for experimentation and simulation in preparation for interpretation of returned data. The use of an accurate simulant will aid the interpretation of data returned from the rover to identify the mineralogy at Oxia Planum. The development of a simulant for Oxia Planum could assist in understanding the preservation and alteration potential of biosignatures at Oxia Planum and identify appropriate biosignature targets for the site. In this paper we present a new simulant, SOPHIA (Simulant for Oxia Planum: Hydrated, Igneous, Amorphous), which represents the mineralogy of Oxia Planum's phyllosilicate-bearing terrain.

1.1 Geological context – Oxia Planum

Oxia Planum is a phyllosilicate-bearing basin (Figure 1b) located on the edge of Mars' crustal dichotomy where the southern highlands of western Arabia Terra meet the northern lowlands, at the southern margin of Chryse Planitia (Figure 1a). Oxia Planum has undergone several periods of fluvial activity associated with Coogoon Vallis and has fluvial systems (Hynek *et al.* 2010; Molina *et al.* 2017; Quantin-Nataf *et al.* 2021; Fawdon *et al.* 2022). The phyllosilicate deposits in the basin, detected by

CRISM and OMEGA (Carter *et al.* 2016; Mandon *et al.* 2021; Brossier *et al.* 2022), occurwhere basaltic minerals, emplaced during the Noachian (4.1 – 3.7 Gya), were altered in subaqueous or subaerial environments either *in situ* or during transport to the basin *via* the surrounding channel network (Quantin-Nataf *et al.* 2021). However, the exact formation mechanism is difficult to deduce from orbital data alone (Carter *et al.* 2016; Mandon *et al.* 2021; Quantin-Nataf *et al.* 2021; Brossier *et al.* 2022). In recent mapping efforts by the Rover Science Operations Working Group (RSOWG), these terrains have been described as the upper and lower bedrock groups (Fawdon *et al.* 2023). This phyllosilicate-bearing unit form part of a widespread network of phyllosilicate deposits that extend to the Chryse Planitia region. While the connection between these deposits is unclear but may represent part of an ancient shoreline of an ocean extending into the northern lowlands if one existed (Figure 1a and c;Parker *et al.* 1989, 1993; Head *et al.* 1998; Clifford and Parker 2001; Ivanov and Head 2001; Dickeson and Davis 2020).

Aqueous episodes in Oxia Planum that post-date the Noachian phyllosilicates (Fawdon *et al.* 2022) are associated with a sedimentary fan deposit containing hydrated silica (Pan *et al.* 2021). The sedimentary fan is thought to have formed during reactivation of the channel systems within Coogoon Vallis (Fawdon *et al.* 2021; Quantin-Nataf *et al.* 2021). An overlying dark deposit caps the phyllosilicates and fan deposits and may have aided their preservation and that of possible biosignatures within them (Quantin-Nataf *et al.* 2021).

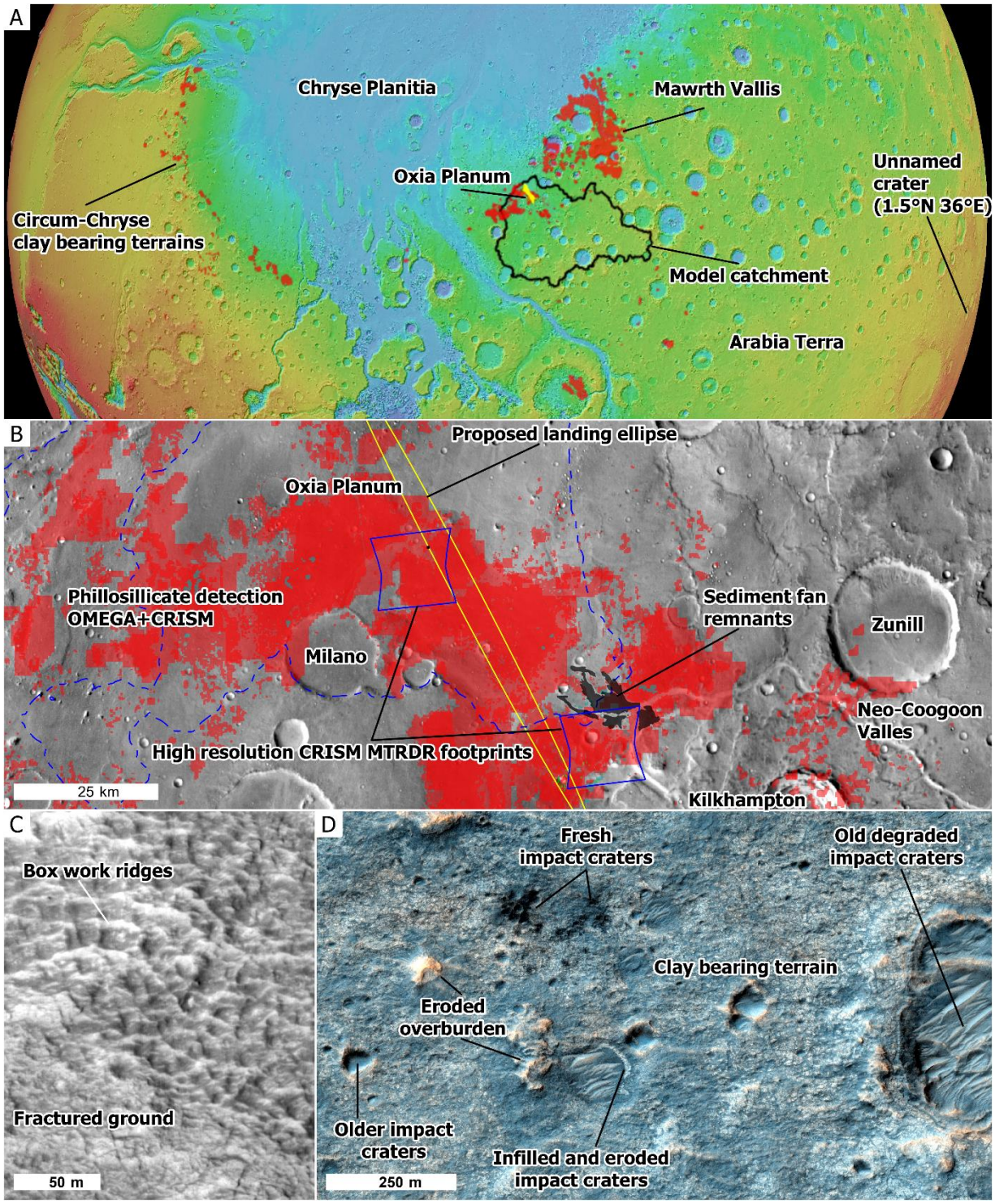

Figure 1: *Context. (A) global context of Oxia Planum, and the Circum-Chryse phyllosilicate-bearing terrains (red; (Carter* et al. *2013, 2015) that SOPHIA represents. Oxia Planum is located on the border of Chryse Planitia, with the Mawrth Vallis region to the east. The un-named crater from Lai* et al. *(2019) is shown to the southeast. (B) The local context of phyllosilicate-bearing terrains as identified by the OMEGA and CRISM (mapping mode) instruments (RED) in the Oxia basin (outlined by the -3000m contour; dashed blue). Also shown are high resolution CRISM Map-Projected Targeted Reduced Data Records (MTRDR) footprints, the sediment fans associated with Neo-Coogoon Vallis and a -3000m contour line delineating 'The Oxia Basin' (Fawdon* et al. *2022) (C) An example of a network of upstanding ridges interpreted to be mineralised veins indicating ground water activity in Oxia Planum (HiRISE (High Resolution Imaging Science Experiment) image ESP_037558_1985). (D) The variety of small (<500 m) scale impact structures that have affected the phyllosilicate-bearing terrains in Oxia*

Planum, which includes contemporary impact craters retaining dark haloes, older partially eroded impact craters, and much older impact structure that have heavily eroded but also show evidence for having been infilled with some now lithified material (HiRISE image ESP_062402_1985_RGB).

1.2 Previous Mars simulants

In the absence of returned samples from Mars, simulants are used to represent its physical, chemical and/or mineralogical properties. Simulants are used in experiments or mission preparation and testing prior to launch and for interpretation of mission data. Martian simulants have been developed to represent global martian mineralogy mainly focusing on the planet's igneous mineralogy: JSC Mars-1 was developed based on spectroscopic data collected by Phobos 2 (Allen *et al.* 1998) and is mostly composed of terrestrial volcanic ash (Allen *et al.* 1998) and the Mojave Mars Simulant (MMS), a geotechnical simulant, was developed using data from the Viking landers (Banin *et al.* 1992), Pathfinder (Moore *et al.* 1999; Foley *et al.* 2003) and the Mars Exploration Rovers (e.g. Klingelhöfer et al. 2004; Morris et al. 2006a, 2006b; Yen et al. 2005), and is composed of mechanically crushed boulders (Peters *et al.* 2008). MSG-1 was designed to represent the Rocknest soil at Gale crater, which is accepted to be representative of a typical basaltic mineral composition on Mars (Bish et al., 2013), containing amorphous material in addition to a crystalline component (Cannon *et al.* 2019).

Although these simulants are globally relevant, there are significant regional differences in geology on Mars, and areas where geological processes (including aqueous alteration) have resulted in diverse mineral assemblages (Bandfield 2002; Mustard 2005; Bibring *et al.* 2006; Wang *et al.* 2006; Ehlmann *et al.* 2008; Carter *et al.* 2010, 2013; Ody *et al.* 2013; Ehlmann and Edwards 2014; Salvatore *et al.* 2018; Osterloo *et al.,* 2008). These are not represented in 'global' Mars simulants meaning those simulants are insufficient for studies investigating specific local environmental conditions or for addressing questions pertaining to the habitability and preservation potential of these terrains.

More recent simulants represent local mineralogy; for example, the S-MRS (Böttger *et al.* 2012) represents a sulphate-rich terrain where sulphates, as detected from orbit and *in situ* (Klingelhöfer *et al.* 2004; Bibring *et al.* 2005; Wang *et al.* 2006), formed during the Hesperian when water evaporated form the martian surface. The OUXX-1 simulants (Ramkissoon *et al.* 2019) were based on four distinct compositions: 1) an early Mars basaltic terrain (based on a basaltic shergottite meteorite composition (Bridges and Warren 2006); 2) a sulphur-rich simulant (based on Paso Robles sulphate-rich samples analysed by the *Spirit* rover at Columbia Hills (Gellert *et al.* 2006; Morris et al. 2006b); 3) a haematite-rich simulant (based on Hematite Slope, a haematite-rich sample at Meridiani Planum analysed by the *Opportunity* rover); 4) a contemporary Mars simulant (based on Rocknest in Gale crater, analysed by the *Curiosity* rover). The Y-Mars simulant (Stevens *et al.* 2018) was developed to represent the composition of the mudstone in the Sheepbed member at Yellowknife Bay, Gale crater, using data from CheMin on board the *Curiosity* rover. The P-MRS simulant (Böttger *et al.* 2012) was developed

to represent the mineralogy of a phyllosilicate-bearing terrain on Mars in which igneous rocks had been altered to phyllosilicate by pH neutral hydrous fluids in a CO_2 rich atmosphere.

Despite these more specific simulants, none have been developed to represent the geological context and mineralogy at Oxia Planum. The P-MRS simulant (Böttger *et al.* 2012) was based on data from across Mars and not an individual region. In addition, it contains 45 % montmorillonite, a phyllosilicate associated with extensive weathering that is not observed to be abundant at Oxia Planum from orbit. Therefore, the development of a simulant specific to Oxia Planum is required so that its precise environment and local variations, specifically phyllosilicate-bearing terrain, can be accommodated. This will help to inform the exploration and data analysis by the rover and studies of this site's astrobiological potential.

2 Simulant design

2.1 Oxia Planum and comparison sites

To initially evaluate the mineralogy needed for SOPHIA, spectral data for Oxia Planum from orbiting spacecraft were considered. The phyllosilicate-bearing terrain at Oxia Planum (Figure 1b) is dominated by Fe/Mg phyllosilicates, as indicated by absorption bands at 1.41, 1.92, 2.30 µm measured by CRISM and OMEGA (Clark *et al.* 1990; Carter *et al.* 2016; Mandon *et al.* 2021; Brossier *et al.* 2022). These absorption bands match best to vermiculite or saponite; vermiculite has absorption bands at 1.42 µm, 2.30-2.31 µm and 2.39 µm (Clark *et al.* 1990; Carter *et al.* 2013; Swayze *et al.* 2018) while Fe-Saponite has absorption bands at 1.40-1.42 µm, 2.30-2.32 µm and 2.4 µm (Treiman *et al.* 2014). Given the similarities in their spectra, it is difficult to distinguish which may be present at Oxia Planum (Mandon *et al.* 2021; Brossier *et al.* 2022).

A further complexity in identifying Oxia Planum's phyllosilicate mineralogy comes from the identification of two spectrally diverse sub-terrains, potentially resulting from the mixing of phyllosilicates with other minerals. In the east, CRISM suggests the phyllosilicate terrain is enriched with olivine, since it is dominated by Fe^{2+}-rich material (Mandon *et al.* 2021; Parkes Bowen *et al.* 2022). In the middle and west of the landing site, CRISM (Mandon *et al.* 2021; Parkes Bowen *et al.* 2022) has suggested the phyllosilicate may be Fe^{3+}-rich, mixed with a Fe-smectite and/or serpentine, chlorite, and/or a carbonate (possibly siderite) identified by a feature at 2.5 µm in the CRISM spectra. As the material to the west and middle of Oxia Planum dominates the landing ellipse for the rover, these terrains will be represented by the SOPHIA simulant. However, as reflectance spectroscopy is highly sensitive to phyllosilicate minerals, the material at Oxia Planum may include a range of compositions from phyllosilicate rich to phyllosilicate poor. To represent a phyllosilicate rich scenario, Fe/Mg

phyllosilicates included as a major component in addition to siderite, Fe-smectite and/or serpentine and chlorite.

However, some minerals cannot be detected within the spectral range of orbiting instruments. For example, CRISM cannot detect non-Fe-bearing felsic minerals as they do not absorb in the Near infrared (Milam *et al.* 2010). Additionally, orbital instruments have a lower spatial resolution (e.g., CRISM 15-19 m/pixel) than rover instruments, meaning some minerals present may not be visible from orbit. To counteract these issues, the Oxia Planum mineralogy has been evaluated in the context of data from the surrounding area. Specifically, CRISM data from the modelled fluvial catchment area of the Oxia Basin (Brossier *et al.* 2022; Turner et al., *Submitted*) (Figure 1b) has been incorporated to specify the mineralogy for the simulant, assuming this material would have been transported into the basin. To better inform decisions regarding the anhydrous (bedrock) mineralogy at Oxia Planum, data from OMEGA and the Thermal Emission Spectrometer (TES) onboard Mars Global Surveyor, taken from the floor of an unnamed crater where bedrock is exposed through an observational window in Arabia Terra (Lai et al., 2019) and olivine, pyroxene and Fe-glass have been detected, were used (Figure 1a).

The minerals suggested to be present at Oxia Planum were compared with other phyllosilicate-bearing sites on the martian surface. Mawrth Vallis was chosen as a comparison site because it contains part of a larger phyllosilicate deposit in the circum Chryse Planitia region, where mineralogy has been extensively studied from orbit (Bishop *et al.* 2008, 2020; Michalski *et al.* 2010; Bishop and Rampe 2016; Lowe *et al.* 2020). At Mawrth Vallis, absorption bands at 1.91 and 2.29-2.31 µm were associated with Fe/Mg phyllosilicates, possibly Fe-smectites and/or vermiculite (Bishop *et al.* 2008; McKeown *et al.* 2009). These Fe/Mg phyllosilicates have been suggested to be spectrally comparable to those at Oxia Planum and in the wider Chryse Planitia region (Figure 1) (McKeown *et al.* 2009; Noe Dobrea *et al.* 2010, 2011; Loizeau *et al.* 2015; Baker 2017; Bishop *et al.* 2020; Lowe *et al.* 2020; Poulet *et al.* 2020). At Mawrth Vallis, Fe/Mg phyllosilicates are overlain by Al-phyllosilicates (montmorillonite and/or beidellite). These overlying phyllosilicates are suggested to have formed through the pedogenesis of the aqueously altered Fe/Mg phyllosilicates (Bishop *et al.* 2008; McKeown *et al.* 2009; Bishop and Rampe 2016; Liu *et al.* 2021). Since Al-phyllosilicates are not present in the areas proposed as the landing site (Carter *et al.* 2016; Mandon *et al.* 2021; Brossier *et al.* 2022), these are not considered and only the Fe/Mg phyllosilicates are used to determine the mineralogy relevant to the simulant.

Yellowknife Bay, Gale crater has also been chosen as a comparison site to Oxia Planum, in particular the Sheepbed member, a mudstone with fine grained phyllosilicates. This mudstone has been analysed (as drill fines) using the XRD on the Curiosity rover. The John Klein (JK) and Cumberland (CB)

drill holes contain trioctahedral Fe/Mg phyllosilicates (Vaniman *et al.* 2014). At Yellowknife Bay, phyllosilicates are suggested to have formed in a closed-system, with circumneutral pH and minimal oxidation (Vaniman *et al.* 2014; Bristow *et al.* 2018) in contrast to other environments at Gale crater, e.g., Glen Torridon, which shows evidence of open-system, acidic and oxidizing environments (Grotzinger 2014; Rampe *et al.* 2020). Similarities between the metre-scale fracturing at Yellowknife Bay, observed by the MastCam instrument (Caswell and Milliken 2017), and the fracturing at Oxia Planum, observed from orbit by HiRISE (Parkes Bowen *et al.* 2020; Apuzzo *et al.* 2022; Parkes Bowen *et al.* 2022), also suggest similarities between these two locations, with the fracturing patterns potentially resulting from similarities in grain size between the two sites or a common fracture formation mechanism such as hydraulic fracturing (Parkes Bowen *et al.* 2020). The use of Yellowknife Bay as a comparison site is limited by the large geographical distance between it and Oxia Planum. In addition, the Fe/Mg phyllosilicates at Yellowknife Bay are much less extensive than those at Oxia Planum and were not detected from orbit (Dehouck *et al.* 2017), meaning the extent of water-rock interactions at Oxia Planum may be much less if phyllosilicates at both sites formed *in situ*. Despite this, the JK and CB samples are used in the design of this simulant as they provide the most similar phyllosilicates to those at Oxia Planum where subsurface *in situ* data is available.

This simulant is designed pre-emptive of rover interpretation of the site and, as such, the design process used a holistic approach to understanding the mineralogy at Oxia Planum, which encompassed its geological context, relationship to the wider Chryse Planitia and similarity to other phyllosilicate terrains on Mars. The location specificity of the simulant means biosignature and habitability studies can be directly relevant to the upcoming *Rosalind Franklin* rover. The simulant is most representative of the lower bedrock groups at Oxia Planum where phyllosilicates have been detected from orbit, and where olivine is less abundant.

2.2 Simulant Mineralogy

Using the data as described in the previous section, decisions regarding the specific mineralogy of the simulant were as follows.

To determine the primary mineralogy of the simulant (the precursor mineralogy to the phyllosilicates and other secondary minerals), data from an unnamed crater in Arabia Terra was used where igneous bedrock is exposed. There, olivine and Ca-pyroxene have been detected (Lai et al., 2019), consistent with CRISM data for the valley walls of Coogoon Vallis in the Oxia Planum catchment area (Turner *et al., submitted*), and thus both minerals selected for inclusion in the SOPHIA simulant. Olivine is also detected in the phyllosilicate -bearing unit at Oxia Planum; the width of the absorption band at Oxia Planum is consistent with either fayalitic (Fe-rich) olivine or large grains of forsteritic (Mg-rich) olivine

(King and Ridley 1987; Mandon *et al.* 2021). As neither is more likely, forsteritic olivine was chosen for the simulant as it was more easily obtained. K-feldspar was detected by *Curiosity* at JK and CB, but not from orbit (Vaniman et al. 2014); however, the abundance of K-feldspar on Mars is thought to be underrepresented in orbital data because of its limited reflectance in the near-IR making it undetectable in CRISM spectra (Milam et al. 2010). For this reason, K-feldspar was also selected for SOPHIA.

For the Fe/Mg phyllosilicate component, vermiculite and saponite were considered as they best matched the dominant phyllosilicate mineralogy at Oxia Planum (Mandon *et al.* 2021; Brossier *et al.* 2022). Either of these minerals could have been chosen, but vermiculite was selected for the simulant because it was more affordable. Spectral features at 2.5 µm suggest the dominant phyllosilicate mineralogy is mixed with a second phyllosilicate mineral possibly serpentine or smectite, with serpentine not easily assessed in the CRISM data (Leask *et al.* 2018). Serpentine was more easily sourced so was included.

As the basaltic minerals at Oxia Planum discussed above are unlikely to be entirely weathered, an intermediate mineral was required. Biotite and chlorite are phyllosilicates from which vermiculite can form. Chlorite forms trioctahedral vermiculite in reducing conditions (Ross and Kodama 1973) and has been detected in association with Fe/Mg phyllosilicates at Mawrth Vallis (Noe Dobrea *et al.* 2010; Bishop *et al.* 2020) and was therefore favoured, however it could not be sourced within budget and at the purity required and was replaced by biotite.

Other minerals commonly formed in association with Fe/Mg phyllosilicates were considered for the simulant. Haematite forms through the oxidative aqueous alteration of basaltic material and is found in low abundance in reducing circumneutral terrains on Mars, including at Yellowknife Bay (Vaniman *et al.* 2014). Iron oxides are also found at Mawrth Vallis (Wray *et al.* 2008) and haematite was identified in the floor of the Coogoon Vallis channel system (Turner *et al. submitted*) that could have been transported by fluvial systems into the Oxia basin (Fawdon *et al.* 2022). As such, haematite was added to the simulant.

Amorphous material was also detected in the JK and CB drill fines and, while the components of this material are unclear, nanophase Fe^{3+} oxides such as ferrihydrite and Fe-glasses have been suggested as candidate components (Dehouck et al. 2014). Fe-glasses have also been detected at the unnamed crater in Arabia Terra, possibly forming in ancient impacts (Lai *et al.* 2019), and are therefore added to the simulant. Ferrihydrite could not be sourced within the budget constraints of the project, so it was substituted by amorphous iron oxyhydroxide, which has similar crystal structure.

Siderite, an Fe-carbonate, has also been suggested to be present alongside the phyllosilicates at Oxia Planum (Mandon *et al.* 2021; Brossier *et al.* 2022). Siderite forms in sedimentary strata laid down under anoxic conditions where Fe^{2+} is present (Lin *et al.* 2020) and is consistent with the lacustrine environment at Oxia Planum. Carbonates have also been detected in association with weathered phyllosilicates at Mawrth Vallis where weathering profiles transition from Fe/Mg phyllosilicates to Al-phyllosilicates (Bultel *et al.* 2019). Fe, Ca-rich Carbonates are suggested to account for the ~1.1-1.7 µm feature in the CRISM spectra at Oxia Planum (Mandon *et al.* 2021), and a Fe/Mg-carbonates is proposed to explain the 2.52 µm feature (Mandon *et al.* 2021; Brossier *et al.* 2022). As such, siderite was added to the simulant. The resulting simulant mineralogy is summarised in Table 1.

Sulphates (gypsum, bassanite and anhydrite) have been proposed to occur in trace amounts in the JK and CB drill fines (4% and 1.6 wt.%, respectively); however, these sulphates are associated with Hesperian-aged surface veins that did not form in association with the phyllosilicate minerals, but were infilled at a different stage (Bibring *et al.* 2006; Ehlmann *et al.* 2011; Vaniman *et al.* 2014),sulphate. Similar sulphate veining may occur at Oxia Planum; however, this simulant will only represent the regions where basaltic rocks are altered to phyllosilicates so sulphates were not added to SOPHIA.

Table 1: *Minerals contained in the SOPHIA simulant*

Ideal Mineral	*Amount to be added (wt. %)*	*Simulant mineralogy (Substitutes in bold)*	*Source*
Vermiculite	*36*	*Vermiculite*	*Dupree Minerals, Uganda*
Serpentine	*3*	*Serpentine*	*Taylor minerals, UK*
Chlorite	*2*	***Biotite***	*Geosupplies, Norway*
Total phyllosilicate	*40*		
Plagioclase	*22*	*Plagioclase*	*Norwegian Edelsplitt AS, Norway*
Orthoclase	*3*	*Orthoclase*	*Geosupplies, Norway*
Pyroxene (Augite)	*15*	*Pyroxene (Augite)*	*Ward Science, Norway*
Olivine	*5*	*Olivine*	*Scangrit, UK*
Total anhydrous minerals	*45*		
Ferrihydrite	*1*	***Amorphous FeOOH***	*Rowaphos*
Fe-glass	*10*	***Fe-Silicate***	*Scangrit, UK*
Total amorphous component	*11*		
Haematite	*1*	*Haematite*	*Geosupplies, UK*
Siderite	*2*	*Siderite*	*Taylor minerals, Wales*

2.3 Determining mineral proportions

As the mineral data form Oxia Planum at this point is purely orbital, there is limited ability to constrain the abundance of minerals from orbit, this data is therefore incorporated with orbital data from relevant sites and with *in situ* quantitative data at Gale Crater in phyllosilicate terrains. Orbital data form OMEGA and TES at the unnamed crater in Arabia Terra have been used to determine the relative abundances of pyroxene, Fe-glass and olivine. Using TES quantitatively can predict mineral abundances to within 5 % accuracy. Here, it is used as a guide to constrain the relative amounts of minerals, such that pyroxene must occur in a higher proportion to Fe-glass, and Fe-glass in a higher proportion to olivine (Lai *et al.* 2019). In the Fe- phyllosilicate terrains at Mawrth Vallis, the mineral abundances on average are; plagioclase 14.57 %, pyroxene 15.76 %, olivine 1.17 %, iron oxides 1.32%, Fe/Mg phyllosilicates 69.11 % (Riu *et al.* 2022). These values are also used to guide the simulant proportions.

To represent a phyllosilicate rich terrain at Oxia Planum, the simulant will contain 35 wt. % phyllosilicate, since non-linear unmixing models deriving relative mineral abundances from orbital data at Oxia Planum suggest an upper limit of 35 % Fe-phyllosilicates in the region (Riu *et al.* 2022). . Finally, the remaining mineral proportions were constrained using quantitative XRD data from CheMin on the *Curiosity* rover for similar minerals at Yellowknife Bay (Vaniman *et al.* 2014). While the geological context of Oxia Planum and Gale crater are likely to be different, CheMin provides the only *in situ* XRD data for Mars that can provide abundances for minerals from samples relevant to rover operations. Siderite was the only mineral that was not comparable at Yellowknife Bay, and so its abundance in the simulant was determined using data from Glen Torridon where it is present at 2.2 wt. % (Rull et al. 2017). The final component abundances are shown in Table 1.

2.4 Determining grain size for the simulant

As this simulant was designed to be a mineralogical simulant, its physical characteristics were not the focus, however since the simulant was to be manufactured, its grain size was considered.

No specific grain size estimations for the phyllosilicates at Oxia Planum have been made but data from the Thermal Emission Imaging System (THEMIS) instrument on Mars Odyssey suggested grain sizes of either coarse sands, or a mixture of coherent rock and finer particulate sand might be anticipated in the phyllosilicate terrains identified by Quantin-Nataf *et al.* (2021) (Gary-Bicas and Rogers 2021). As such, grain sizes for SOPHIA were chosen based on grain sizes at Yellowknife Bay, given the possible similarities between the depositional environments of the two locations. At Yellowknife Bay, the Mars Hand-held Imager (MAHLI) identified grain sizes between 44 and 60 μm in diameter for the phyllosilicate-bearing rocks in the Sheepbed member (Rivera-Hernández *et al.* 2019). Grain size estimations are also provided by point-to-point chemical variabilities in ChemCam Laser Induced

Breakdown Spectroscopy (LIBS) data at Gale crater, which has suggested grains within Sheepbed member mudstones are <62.5 µm, constituting a silt-clay sediment (Rivera-Hernández *et al.* 2019). Analysis of MAHLI images on a pixel-by-pixel basis suggest that material at Gale crater may be dominated by grains as small as 20 µm (Schieber 2018). In addition, possible similarities in grain size are suggested by the scale of fracturing (Parkes Bowen *et al.* 2020). On Earth, the grain size of phyllosilicate minerals typically fall into the 'clay' grain size classification, typically measuring <2 µm in diameter (Brindley 1983).

3 Simulant development

3.1 Test samples

Once the simulant components were identified, test samples were acquired from the suppliers (Table 1) to confirm their mineralogy and assess their purity prior to purchasing the required quantities. The identification of any accessory mineral phases allowed the proportions of each component to be adjusted to achieve the desired target simulant mineralogy. Each sample was analysed using scanning electron microscopy-energy dispersive spectroscopy (SEM-EDS), which confirmed the mineralogy, elemental composition and the homogeneity of the samples (see section 3.1.1). Once the mineralogy of the samples was confirmed, the simulant components were ordered in bulk to make 30 kg of simulant.

3.2 Simulant production

The component minerals were split, crushed, milled, and sieved at the crushing facility at The Open University, UK. A rock splitter was used to split samples larger than 4 cm^3 (orthoclase, serpentine, and augite). Samples were then crushed in a jaw crusher to a size of ~0.5-3 mm in diameter (orthoclase, serpentine, augite, siderite, haematite). The platy crystal habit of biotite meant it could not be crushed in the jaw crusher and was instead broken into small pieces using a rock hammer. A Retsch PM400 planetary ball mill was used to further crush all simulant components to a fine sand, which were then sieved to <212 µm. This grain size was chosen as the time required to mill and sieve tens of kg to <60 µm was not feasible. The mineral components were mixed and homogenised in large mixing bowls and subsampled using the coning and quartering technique (Campos and Int 2017). This contamination during simulant production was contained by cleaning splitting and crushing milling machinery first with decon 90 followed by acetone. Ball mill containers could be removed from the crushing facility so were further solvent cleaned using dichloromethane and methanol with sonication to remove a range of organics. The simulant was stored in glass jars and the lids sealed with foil to prevent contamination.

4 Simulant Characterisation

The following Characterisation data is available at (10.21954/ou.rd.22219903). Photographs of the mineral components in their supplied, milled and sieved states and at ×50 magnification when polished and embedded in epoxy are provided in Table S1.

4.1 Scanning electron microscopy - energy dispersive spectroscopy (SEM-EDS)

SEM-EDS analysis was conducted on test samples (~3 × 3 cm) to confirm their mineralogy, elemental composition and homogeneity. The samples were embedded into epoxy resin blocks of 4 cm diameter, polished flat and carbon coated before analysis. These samples were analysed using a FEI Quanta 200 3D scanning Electron Microscope (SEM), equipped with an Oxford Instruments Energy Dispersive X-ray detector (EDS), using a 20 kV electron beam. The working distance was 15 mm. EDS chemical mapping was coupled with backscatter electron (BSE) imaging. Bulk chemical data for the test samples were collected using randomised large-area mapping, whereby multiple maps were acquired over the surface at regularly intervals and collated. This provided a detailed composition representative of the test sample as a whole, negating the sampling bias associated with choosing a specific location to map. This provided an overview of the sample mineralogy and supplied semi-quantitative information on the proportion of mineral phases in the samples. SEM-EDS results for components are shown in Table 2. To assess the simulant's bulk chemistry, an SEM-EDS map was taken using the parameters described above. The bulk chemical composition based on large area chemical mapping is shown in Table 3. The map with identified minerals is shown in Figure 2.

392

393 ***Table 2:*** *SEM-EDS data for the component minerals for the simulant (in the test samples), identifying dominant mineral phases and contaminant mineral phases.*

				Oxide percentages in each mineral phase											
	Simulant component	***Mineral phase***	***%***	***MgO***	***Al_2O_3***	***SiO_2***	***K_2O***	***FeO***	***Fe_2O_3***	***Na_2O***	***CaO***	***Ti_2O_2***	***MnO***	***Cr_2O_3***	***CO_2***
1	*Vermiculite*	*Fe/mg-vermiculite*	*91*	*20.53*	*21.75*	*43.45*	*5.53*	*7.21*	*-*	*-*	*0.45*	*1.11*	*-*	*-*	*-*
		Al-vermiculite	*6*	*12.33*	*59.56*	*21.03*	*2.18*	*4.62*	*-*	*-*	*-*	*-*	*-*	*-*	*-*
		Mg-vermiculite	*3*	*29.30*	*12.75*	*44.23*	*-*	*7.13*	*-*	*-*	*-*	*-*	*-*	*-*	*-*
2	*Anorthosite*	*labradorite*	*72*	*-*	*26.35*	*56.87*	*0.58*	*-*	*0.32*	*6.01*	*9.87*	*-*	*-*	*-*	*-*
		Oligoclase	*25*	*-*	*25.30*	*62.28*	*1.46*	*0.19*	*-*	*8.32*	*2.46*	*-*	*-*	*-*	*-*
		Sanidine	*2*	*-*	*34.66*	*51.91*	*9.15*	*0.87*	*-*	*1.89*	*1.52*	*-*	*-*	*-*	*-*
		Albite	*<1*	*-*	*19.90*	*69.17*		*-*	*-*	*10.93*	*-*	*-*	*-*	*-*	*-*
		*Bytownite**	*<1*	*-*	*32.68*	*47.69*	*5.63*	*0.97*	*-*	*0.89*	*12.15*	*-*	*-*	*-*	*-*
		Unknown	*<1*	*11.92*	*24.59*	*42.76*	*0.73*	*16.03*	*-*	*-*	*3.96*	*-*	*-*	*-*	*-*
		Sanidine	*<1*	*3.88*	*32.62*	*48.12*	*9.73*	*4.54*	*-*	*-*	*1.12*	*-*	*-*	*-*	*-*
3	*Orthoclase*	*Orthoclase*	*92*	*-*	*18.80*	*64.93*	*14.53*	*-*	*-*	*1.74*	*-*	*-*	*-*	*-*	*-*
		Plagioclase	*8*	*-*	*21.34*	*67.26*	*1.56*	*-*	*-*	*9.85*	*-*	*-*	*-*	*-*	*-*
4	*Haematite*	*Haematite*	*87*	*-*	*-*	*0.01*	*-*		*98.99*	*-*	*-*	*-*	*-*	*-*	*-*
		Haematite	*7*	*-*	*--*	*2.79*	*-*		*97.22*	*-*	*-*	*-*	*-*	*-*	*-*
		*Macaulayite**	*6*	*-*	*14.28*	*9.21*	*-*	*76.51*	*-*	*-*	*-*	*-*	*-*	*-*	*-*
5	*Siderite*	*Siderite*	*99*	*-*	*-*	*-*	*-*	*52.14*	*-*	*-*	*0.74*	*-*	*1.32*	*-*	*45.80*
		Calcite	*1*	*-*	*-*		*-*	*3.37*	*-*		*44.9*	*-*	*0.37*		*51.33*
6	*Amorphous β-FeOOH*	*Amorphous β-FeOOH*	*100*	*-*	*-*	*-*	*-*	*-*	*100*	*-*	*-*	*-*	*-*	*-*	*-*
7	*Serpentine*	*Lizardite*	*75*	*40.59*	*3.13*	*49.31*	*-*	*6.79*	*-*	*-*	*-*	*-*	*-*	*-*	*-*
		Serpentine	*34*	*44.60*	*-*	*47.3*	*-*	*-*	*-*	*-*	*0.35*	*0.22*	*-*	*-*	*-*
		Olivine	*1*	*28.34*	*-*	*28.84*	*-*	*42.83*	*-*	*-*	*-*	*-*	*-*	*-*	*-*
		*Tremolite**	*<1*	*31.25*	*-*	*54.38*	*-*	*4.41*	*-*	*-*	*9.96*	*-*	*-*	*-*	*-*
8	*Pyroxene*	*Pyroxene (omphacite)*	*47*	*-*	*32.18*	*51.77*	*5.48*	*-*	*-*	*7.83*	*2.74*	*-*	*-*	*-*	*-*
		Pyroxene (augite)	*39*	*11.48*	*-*	*51.90*		*9.40*	*-*	*-*	*23.99*	*3.28*	*-*	*-*	*-*
		Pyroxene (pigeonite)	*9*	*29.92*	*-*	*34.41*	*0.01*	*34.17*	*-*	*-*	*0.06*	*0.01*	*0.07*	*-*	*-*

		*Amphibole (kaersuite)**	*5*	*6.41*	*17.12*	*47.47*	*1.52*	*7.80*	-	*5.08*	*12.38*	-	-	-	-
		Orthoclase	*<1*	-	*19.94*	*62.84*	*12.74*	*0.90*	-	*2.53*	*0.75*	*0.31*	-	-	-
9	*Fe-silicate*	*Fe-silicate*	*94*	-	*4.52*	*38.84*	*0.58*	*51.43*	-	-	*4.25*	*0.38*		-	-
		Fe,Ca-Silicate	*6*	*3.23*	*4.28*	*33.01*		*43.34*	-	-	*16.13*				-
10	*Olivine*	*Mg rich olivine (chrysolite)*	*98*	*50.17*	-	*42.27*	-	*7.57*	-	-	-	-	-	-	-
		*Hornblende**	*1*	*22.87*	*4.77*	*53.79*	-	*3.84*	-	-	*12.70*	-	-	*2.03*	-
		Pyroxene (enstatite)	*<1*	*33.18*	-	*63.36*	-	*3.47*	-	-	-	-	-	-	-
11	*Biotite*	*Biotite*	*99*	*7.52*	*16.14*	*39.17*	*9.61*	*24.21*	-	-	*0.08*	*2.78*	*0.49*	-	-
		Biotite	*<1*	*6.98*	*18.57*	*41.59*	*5.08*	*25.33*	-	-	*0.64*	*1.81*	-	-	-
		Unknown	*<1*	*2.14*	*27.43*	*49.52*	*10.5*	*9.1*	-	-		*1.32*	-	-	-

**The identity of these minerals is speculative as they could not be conclusively determined. They are present in small enough amounts as to not affect the overall mineralogy of the simulant.*

Table 3: *Bulk wt.% oxides based on the SEM-EDS and XRF analysis of the bulk simulant.*

Oxide	***Calculated chemistry based on mineral input***	***XRF %***	***SEM-EDS %***
SiO_2	*48.28*	*46.42*	*48.16*
TiO_2	*0.64*	*0.51*	*0.69*
Al_2O_3	*17.96*	*11.42*	*14.13*
Fe_2O_3/FeO	*12.89*	*13.49*	*12.82*
MnO	*0.03*	*0.14*	*n/a*
MgO	*8.28*	*13.77*	*15.79*
CaO	*4.08*	*6.07*	*4.95*
Na_2O	*2.05*	*1.73*	*n/a*
K_2O	*2.84*	*2.98*	*3.46*
P_2O_5	*n/a*	*0.051*	*n/a*
SO_3	*n/a*	*0.094*	*n/a*
LoI		*3.73*	*n/a*

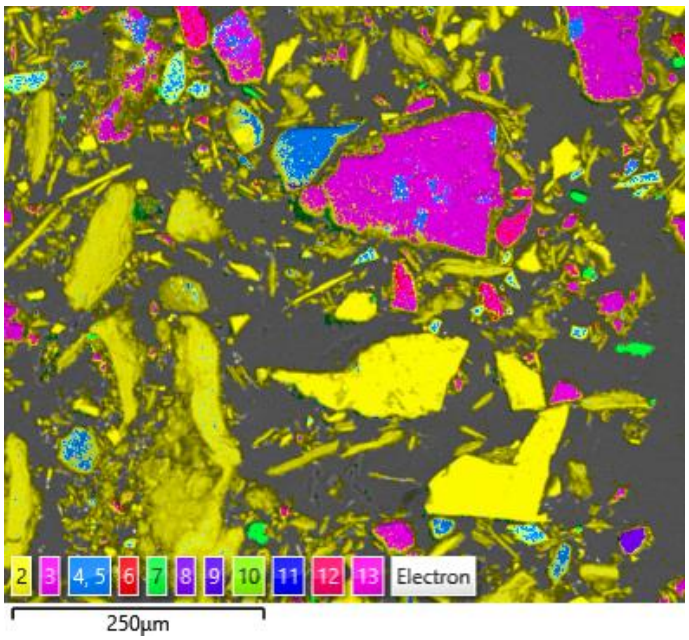

Figure 2: False-colour SEM-EDS map showing the different components in the bulk simulant based on the elements detected. *(2) Vermiculite (3) Oligoclase (4, 5) Pyroxene (6) Orthoclase (7) Haematite/Siderite/ Amorphous β-FeOOH (9) Olivine.*

4.2 Raman Spectroscopy

Raman spectroscopy was used to confirm the mineral phases present in each of the test samples. A Horiba Jobin-Yvon HR800 spectrometer was used, which was equipped with an Ar ion laser (of wavelength 514 nm) as the excitation source. This wavelength was used to ensure the results were comparable to the Raman Laser Spectrometer (RLS) instrument aboard the *Rosalind Franklin* rover (Rull *et al.* 2017). To prevent the laser burning the samples and to prevent thermally-induced florescence, a 10% neutral density filter (N.D.) was used, reducing the power output at the microscope

410 objective. A ×10 microscope objective was used to achieve a spot size of 2.5 µm, while a 600
411 grooves/mm diffraction grating gave a spectral resolution of 1.5 cm^{-1}. A montage (1000 × 1000 µm)
412 was acquired, and a map consisting of 100 spectra was collected for this area. Raman spectra were
413 analysed using the *Labspec* 6 software by applying a baseline correction and then a peak fitting
414 function using a Gaussian-Lorentzian profile to identify peak positions and peak widths (taken at full
415 width half maxima). Minerals were identified using characteristic bands reported in the literature and
416 the RRUFF database (Lafuente *et al.* 2015). The characteristic peaks for the phases identified are
417 presented in Table 4. The Raman spectrum for the bulk simulant is shown in Figure 3.

418 ***Table 4:*** *Confirmation of mineral composition by Raman spectroscopy*

Sample	***Mineral phase***	***Experimental peaks (Raman shift (cm^{-1})***	***Reference***
Vermiculite	*Vermiculite*	*195, 360, 548, 682*	*Lafuente et al., (2015)*
Serpentine	*Lizardite*	*223,298, 408 678*	*Lafuente et al., (2015)*
	Chrysotile	*277, 414, 690, 1033*	*Lafuente et al. (2015)*
Biotite	*Biotite*	*231 389 686*	*Wang et al., 2015)*
	Phlogopite	*234, 303, 389, 697, 827, 863*	*Wang et al., (2015)*
Synthetic Fe-silicate		*920*	
Plagioclase (Anorthosite)	*Labradorite*	*207. 298, 424, 488, 510*	*Lafuente et al., (2015)*
	Oligoclase	*209, 282, 488, 515, 770, 825, 1126*	*Lafuente et al., (2015)*
Orthoclase	*Orthoclase*	*166, 267, 288, 460, 477, 518, 756, 816, 1142*	*Lafuente et al., (2015)*
Pyroxene		*327, 403, 488, 507, 658, 819, 857, 1013*	
Olivine	*Olivine*	*157, 347, 400, 637, 816, 855, 915, 945, 1114, 1602*	*Berlanga et al., (2019)*
	Pyroxene	*234, 347, 678, 1017, 1602*	
Haematite	*Haematite*	*225, 285, 414, 469, 617, 1322*	*Lafuente et al., (2015)*
Amorphous β-FeOOH	*Amorphous β-FeOOH*	*160, 218, 284, 893*	*n/a*
Siderite	*Siderite*	*187, 283, 1087*	*Lafuente et al. 2015)*

419

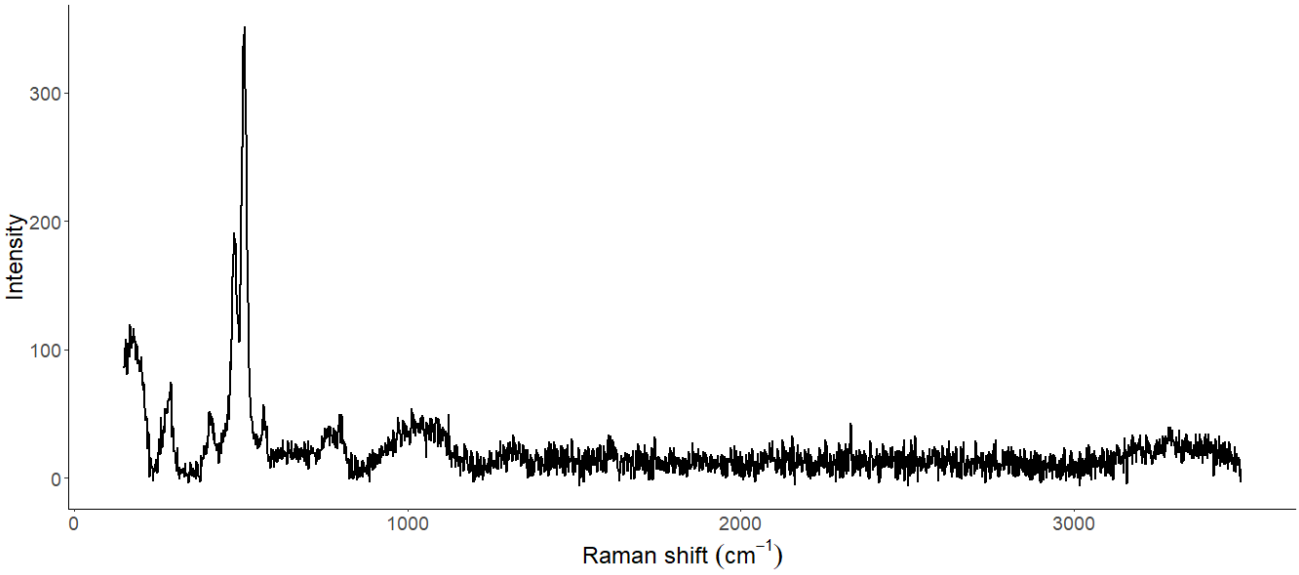

420

421 ***Figure 3*** *Raman spectrum for the SOPHIA simulant showing peaks at 186 and 512 cm^{-1} associated with*
422 *phyllosilicates; florescence from 1000 cm^{-1} to 3500 cm^{-1} is also due to the presence of phyllosilicates, removed*
423 *with baseline correction.*

4.3 Electron microprobe analysis (EMPA)

EMPA was used to obtain quantitative chemical data for the dominant mineral phases in each test sample. A Cameca SX100 microprobe equipped with five spectrometers was used for analysis. Samples were analysed using a 10 µm beam diameter, using a 20 kV accelerating voltage and 20 nA current. The probe was programmed to measure elemental concentrations of K, Mn, Ca, Fe, Si, Mg, Cr, Ti, Al, Si as these elements were shown to be present in the samples with SEM-EDS. EMPA can determine the chemical composition with higher sensitivity than SEM-EDS with a spectral resolution of roughly an order of magnitude higher. Standards within the software were used to calibrate the probe prior to the unknown compositions being analysed. The vermiculite samples could not be analysed by EMPA because of the challenges associated with preparing polished blocks(Fitzpatrick 1984), and because of damage to the sample caused by the interaction with the electron beam; these are recognised challenges associated with analysing phyllosilicate minerals (Biroň *et al.* 1999). The EMPA results are shown in Table 5.

Table 5: Electron microprobe characterisation of the simulant components

Component	*Mineral Phase*	*K_2O*	*MnO*	*FeO*	*Fe_2O_3*	*CaO*	*Na_2O*	*Al_2O_3*	*SiO_2*	*MgO*	*Cr_2O_3*	*TiO_2*	*P_2O_5*	*SO_2*	*H_2O*
Vermiculite	*Vermiculite**	*2.5*	*0.02*	*3.13*	*-*	*0.02*	*0.43*	*5.77*	*23.67*	*13.80*	*0.01*	*0.55*	*-*	*0.28*	*49.63*
Plagioclase	*Plagioclase*	*4.29*	*-*	*0.39*	*-*	*3.27*	*6.13*	*27.45*	*58.06*	*0.20*	*-*	*0.01*	*0.02*	*0.01*	*-*
Orthoclase	*Orthoclase*	*16.3*	*-*	*0.03*	*-*	*0.04*	*0.65*	*18.45*	*64.48*	*-*	*-*	*0.03*	*-*	*-*	*-*
Haematite	*Haematite*	*-*			*98.67*	*-*	*-*	*-*	*-*	*-*	*-*	*-*	*-*	*-*	*-*
Siderite	*Siderite*	*-*	*2.03*	*92.41*	*-*	*1.44*	*-*	*4.00*	*0.05*	*0*	*-*	*-*	*-*	*-*	*-*
Amorphous β-FeOOH	*Iron Oxide*	*-*	*-*	*-*	*72.00*	*-*	*-*	*-*	*-*	*-*	*-*	*-*	*-*	*-*	*28.00*
Serpentine	*Lizardite*	*0.01*	*0.24*	*7.22*	*-*	*0.09*	*-*	*0.86*	*40.1`*	*36.05*	*0.02*	*0.04*	*0.01*	*0.03*	*15.32*
	Tremolite	*0.02*	*0.09*	*3.21*	*-*	*11.92*	*0.63*	*3.48*	*53.34*	*22.75*	*0.46*	*0.35*	*0.02*	*0.01*	*3.72*
Pyroxene	*Omphacite*	*4.02*	*0.01*	*0.47*	*-*	*2.85*	*8.08*	*26.3*	*58.09*	*0.03*	*-*	*0.09*	*-*	*-*	
	Augite	*-*	*0.17*	*8.72*	*-*	*22.85*	*0.65*	*7.67*	*46.2*	*10.78*	*0.05*	*2.86*	*0.03*	*-*	
	Orthoclase	*10.8*	*-*	*0.14*	*-*	*0.72*	*4.12*	*19.37*	*64.75*	*-*	*-*	*0.08*	*-*	*-*	
	Iron silicate	*9.12*	*0.19*	*19.85*	*-*	*0.90*	*0.6*	*13.62*	*37.6*	*11.3*	*0.01*	*6.79*	*-*	*0.01*	
	Plagioclase	*0.56*	*0.01*	*0.30*	*-*	*0.49*	*13.08*	*27.79*	*57.31*	*0.05*	*-*	*0.03*	*0.37*	*-*	
	Fe-Ti Oxide	*0.01*	*1.23*	*73.1*	*-*	*0.06*	*-*	*1.79*	*0.16*	*0.44*	*0.24*	*22.98*	*-*	*-*	
Fe-silicate	*Fe-silicate*	*0.58*	*0.55*	*48.39*	*-*	*4.52*	*0.61*	*4.75*	*38.05*	*1.26*	*0.25*	*0.26*	*0.22*	*0.57*	*0.58*
Olivine	*Olivine*	*-*	*-*	*7.19*	*-*	*-*	*-*	*-*	*41.15*	*51.25*	*-*	*-*	*-*	*-*	*-*
	Olivine	*-*	*-*	*6.17*	*-*	*-*	*-*	*-*	*46.76*	*46.85*	*-*	*-*	*-*	*-*	*-*
	Serpentine	*0.01*	*0.01*	*2.77*	*-*	*0.01*	*-*	*16.33*	*38.29*	*38.64*	*3.99*	*0.03*	*0.01*	*0.02*	*-*
Biotite	*Biotite*	*9.55*	*0.48*	*24.18*	*0.03*	*0.08*	*15.22*	*36.44*	*7.48*	*-*	*2.53*	*-*	*0.05*	*3.95*	*9.55*

*Vermiculite could not be analysed accurately because the samples could not be polished without plucking out the soft grains, resulting in an irregular surface that meant the probe was difficult to focus.

4.4 X-Ray Florescence Spectroscopy

X-Ray Florescence Spectroscopy (XRF) was used to provide quantitative chemical data for the bulk simulant. This was conducted at the University of Leicester, UK, using a Rigaku ZSX PrimusIV WD-XRF. Homogenised samples were crushed to <53 µm in diameter, and ignited powders were used to prepare fused silica beads on which major elements were determined, with a sample to flux ratio of 1:7.5 66% Li metaborate: 34% Li tetraborate flux. Results are quoted as component oxide weight percent (wt.%) and recalculated to include Loss on Ignition (LOI). A PANalytical Axios Advanced WD-XRF was used to analyse trace elements. Samples were made into 32 mm diameter powder pellets produced by mixing 10 g of ground simulant with 20-25 drops of a 7% PVA solution (Moviol 8-88) and pressed at 152 MPa. The XRF data is shown in Table 3. In addition, the XRF results can be used to assess the Chemical Index of Alteration (CIA) for the simulant to understand the type of alteration environment (Nesbitt and Young 1982) it represents on Mars (Equation 1), giving a CIA of 51 for the simulant, usually associated with an environment bordering between an open and closed system.

$$CIA = 100 \times \frac{Al_2O_3}{Al_2O_3+CaO+Na_2O+K_2O} \quad \text{(Equation 1)}$$

4.5 Near-IR Spectroscopy

Near-IR spectroscopy was used to characterise the bulk simulant, which allowed the data to be compared to the CRISM spectra of Oxia Planum and can be used to compare the spectral similarities between the simulant and Oxia Planum from orbit before the *Rosalind Franklin* rover lands. The data can also be used to compare to the rover's ISEM (Korablev *et al.* 2017), MicrOmega (Bibring *et al.* 2017) and Ma_MISS (contact in the drill hole) instruments (De Sanctis *et al.* 2022). Near-IR spectra were obtained using an Avantes AvaSpec-NIR512-2.5-HSC-EVO (with thermoelectric cooling) using a 100 lines/mm grating with a 1350-2500 nm usable spectral range. These parameters provide a spatial resolution of 7.2-50 µm. The spectrometer was used in conjunction with AvaSoft 8 software where calibration of the instrument and smoothing of data was performed. Calibration was performed using white and dark references before acquiring spectra. Once spectra were acquired, standard correction smoothing was performed as a standard procedure. An example spectrum for the simulant is shown in Figure 4 (blue spectrum). The CRISM spectra at Oxia Planum are also shown for comparison (black spectra).

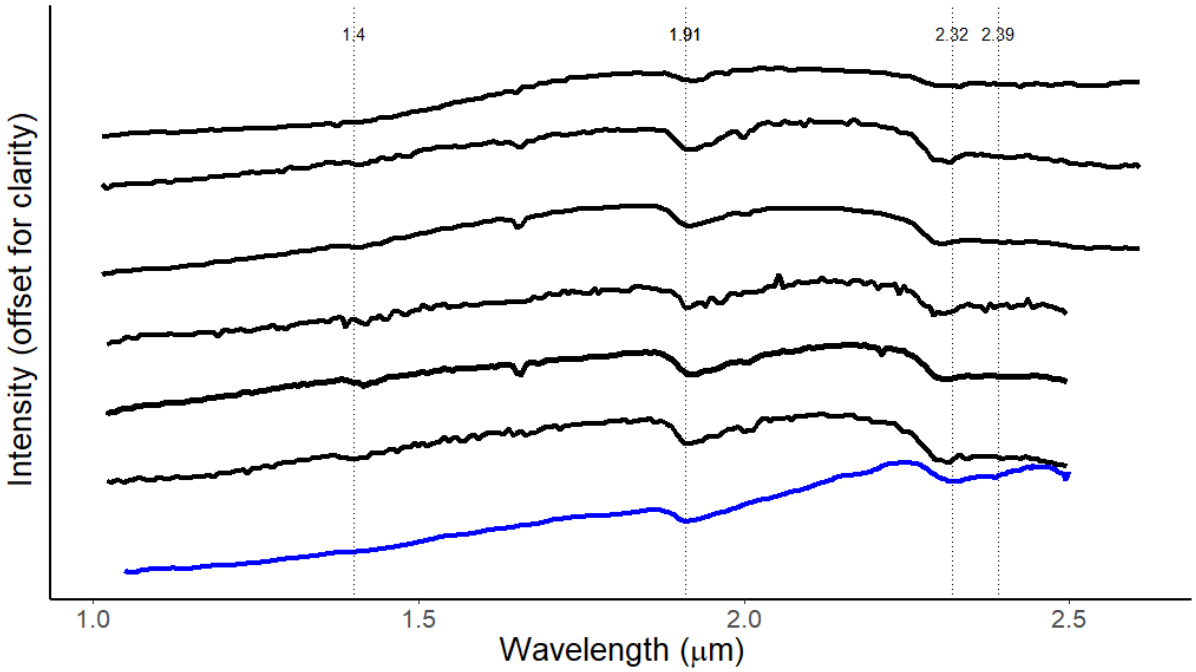

Figure 4: *In black, the Near-IR spectrum for the bulk simulant shows absorption bands shown using dotted lines at 1.92 and 2.3 µm associated with hydration, and absorption at 2.5 µm is possibly due to the mixing of vermiculite with siderite and/or serpentine (blue spectrum . Three Near-IR spectra from Oxia Planum taken by the CRISM instrument show absorption at 1.9 µm and 2.3 µm (shown in black; Turner and Bridges 2017; Mandon* et al. *2021).*

4.6 X-Ray Diffraction (XRD)

X-Ray diffraction (XRD) was used to assess the mineralogy of the bulk simulant, quantify its composition and verify its homogeneity. Qualitative analysis was conducted at the Open University, using a Siemens D5000 taking measurements from 5 to 90 degrees in 0.02 step. This was repeated on three aliquots of simulant to ensure the simulant was homogenous (Figure 5).

XRD analysis was conducted on each of the component minerals and the diffraction patterns form this analysis were combined using FULLPAT software (Chipera and Bish 2002) to provide a theoretical diffraction pattern for the combined simulant. This analysis is compared to the XRD analysis for the bulk spectra in Figure 6. Rietveld refinement was also applied to the diffraction pattern to acquire quantitative data (Table S2). In addition, XRD analysis, to fully quantify the amorphous material, was run at Sheffield Hallam University using a PANalytical Empyrean X-ray Powder Diffractometer. A 3.45 w% of NIST SRM 640e silicon XRD standard powder was added to the simulant for comparison to the simulant's amorphous content.

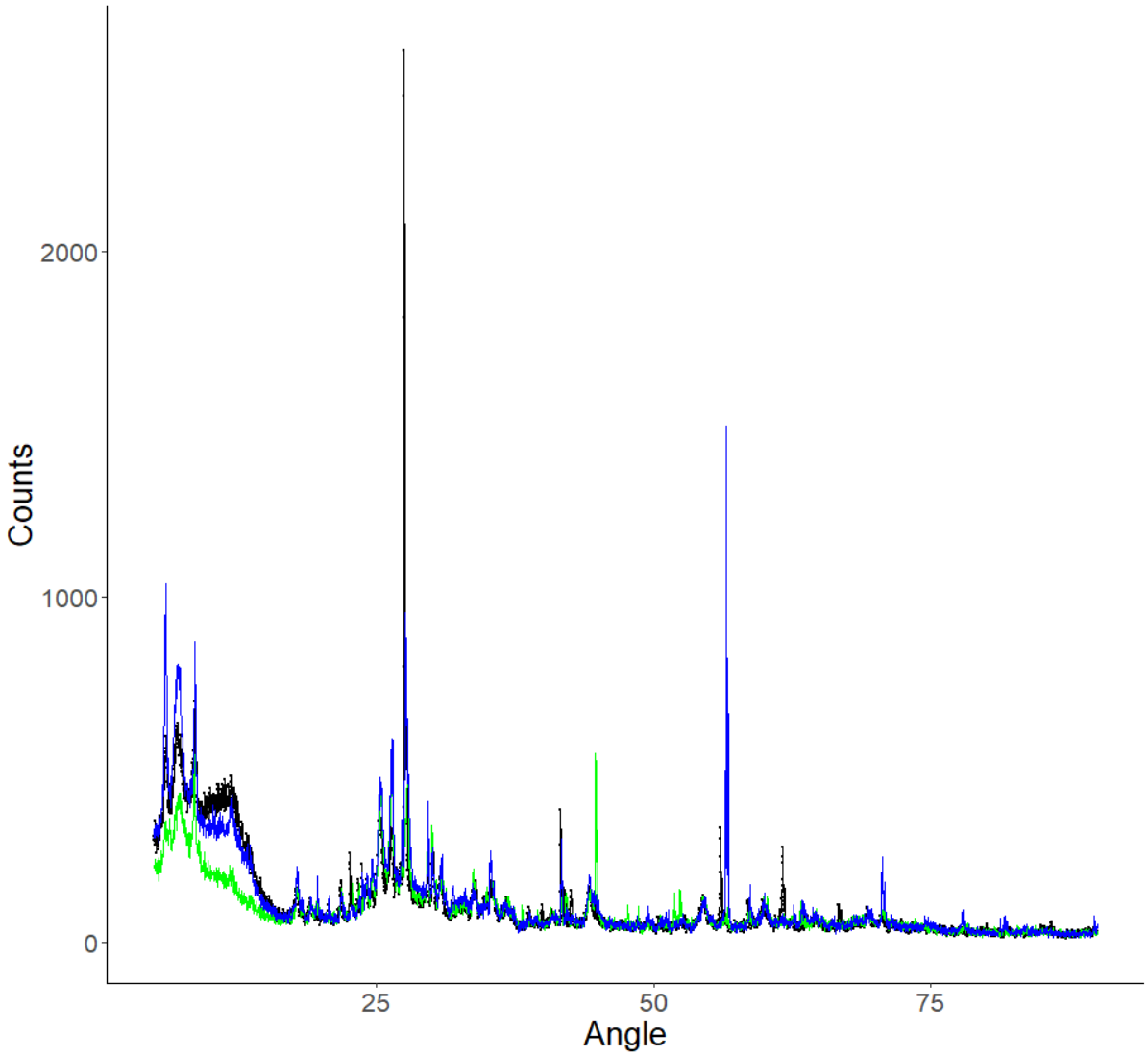

Figure 5: *XRD diffraction pattern for 3 aliquots of simulant.*

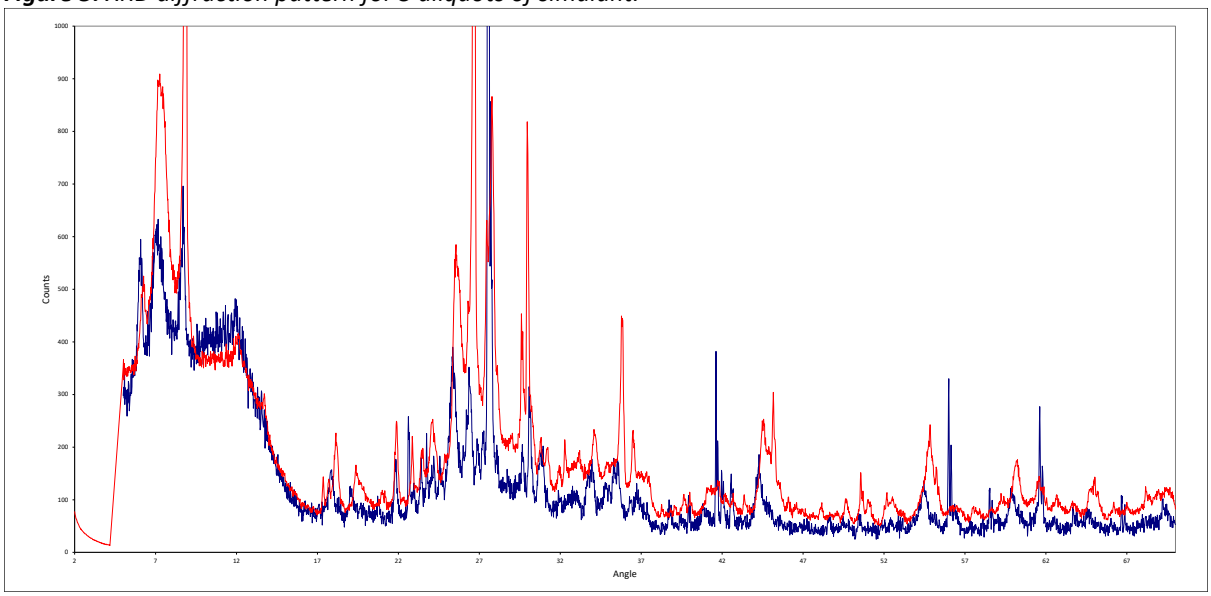

Figure 6: *XRD diffraction patterns showing the analysis of the bulk simulant (blue) and the theoretical pattern for the sum of the components (red).*

4.7 Mössbauer Spectroscopy

Mössbauer spectroscopy (e.g. Gütlich and Schröder 2012) was used to analyse the Fe^{2+}/Fe^{3+} ratio of the bulk simulant by characterising the mineralogy of the Fe-bearing minerals in the simulant (vermiculite, siderite, amorphous β-FeOOH, haematite and Fe-silicate). Mössbauer was used onboard the Mars Exploration Rovers (MER) *Spirit* and *Opportunity* (Klingelhöfer *et al.* 2003) that analysed surfaces materials in Gusev crater and at Meridiani Planum (Klingelhöfer *et al.* 2004; Morris *et al.* 2006a, 2006b, 2019).

Mössbauer analysis of the simulant was conducted at the Mössbauer Spectroscopy laboratory for Earth and Environment (MoSEE) at the University of Stirling. Aliquots of the bulk simulant (116 mg), and the individual components Fe-silicate glass (115 mg), β-FeOOH (103 mg) and vermiculite (110 mg) were placed into acrylic glass sample holders (~1.3 cm circular diameter) and measured at three different temperatures (room temperature, 77 K, 4.2 K) with a standard transmission spectrometer (Wissel, Germany) attached to a closed-cycle helium gas cryostat (DRY ICE 4K, ICEoxford, UK). The instrument uses 14.4 keV gamma radiation emitted by a ^{57}Co in Rh matrix source in constant acceleration mode (triangular waveform). Spectra were calibrated against a spectrum of α-iron foil (25 µm thickness) at room temperature. Spectra were evaluated with Recoil (Ottawa, Canada) using the Voigt-based fitting routine (Rancourt and Ping 1991). No f-factor correction was applied. Mössbauer spectra are shown in Figure 7 and Mössbauer parameters are listed in Table S3.

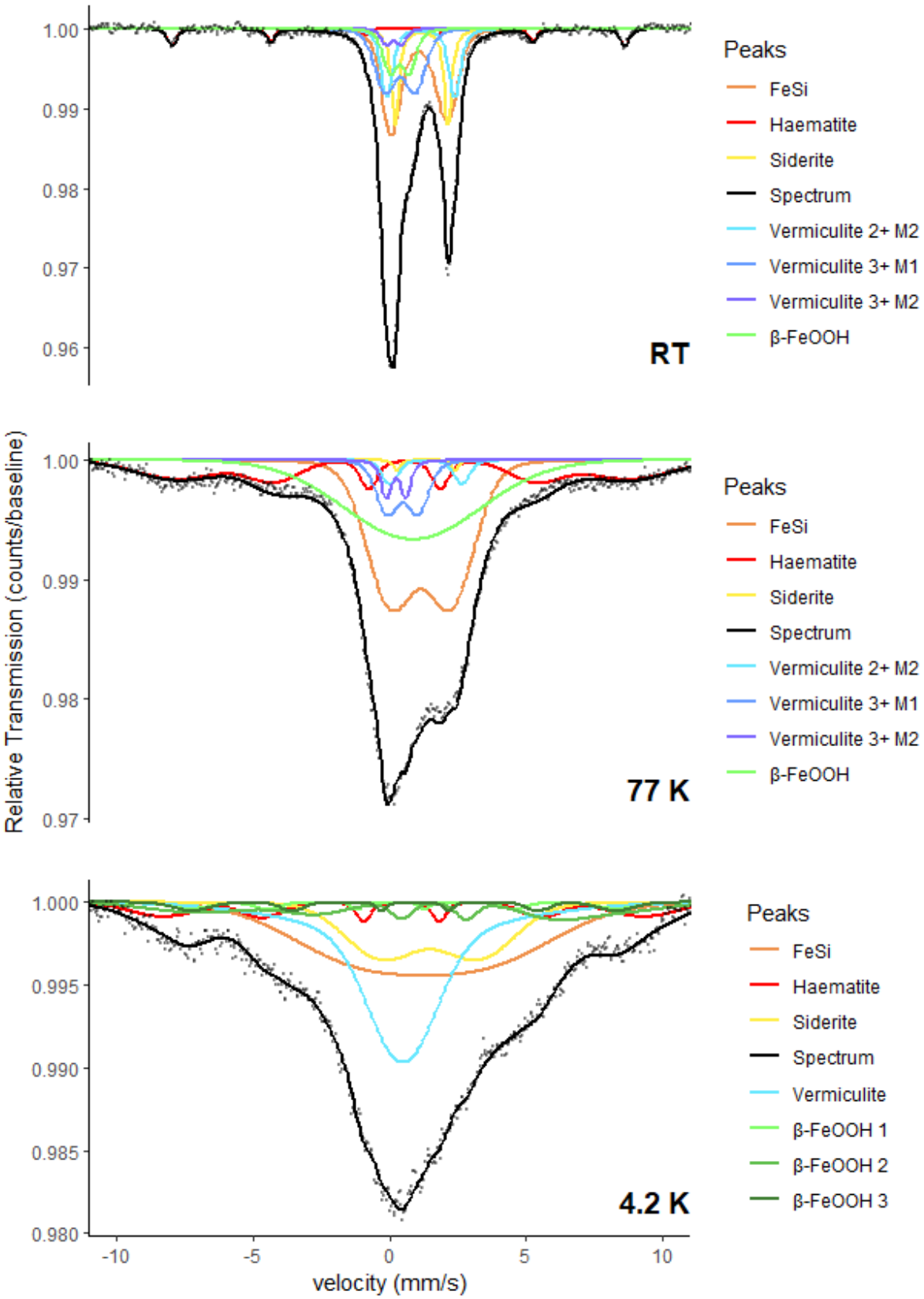

514

515 ***Figure 7:*** *Mössbauer spectra for simulant and iron containing components. A – Spectrum measured at room*
516 *temperature. B – Spectrum measured at 77 K. C – Spectrum measured at 4.2 K.*
517

4.8 Physical and mechanical properties

Characterisation of the simulant's physical properties was conducted by K4soils (K4 Soils testing laboratory, Watford, UK), using 400 g of the homogenised simulant with a size fraction of ≤ 212 µm.

The bulk density (ρ) of the simulant was calculated by performing linear measurements (Hvorslev, 1970) and was calculated using Equation (2)

$$\rho = \frac{400\,m}{\pi D^2 L} \quad \text{(Equation 2)}$$

where, m is mass (kg), D is mean diameter of cylinder (m), and L is mean length (m). Bulk density was found to be 1150 kg m^{-3}.

The simulant's particle density (ρ_s) was measured using the small pycnometer method and was found to be 2.91 kg m^{-3}.

Porosity was calculated using the bulk density and particle density measurements by determining specific gravity (G_s) and void ratio (e) using Equations (3) – (5):

$$G_s = \frac{\rho_s}{\rho_w} \quad \text{(Equation 3)}$$

$$e = G_s \frac{\rho_w}{\rho} - 1 \quad \text{(Equation 4)}$$

$$n = \frac{e}{(1+e)} \quad \text{(Equation 5)}$$

where, ρ_s is the particle density and ρ_w is the density of water (1000 kg m^{-3}), and ρ is the bulk density. The simulant porosity was 61%.

The grain size distribution across 100 g of the bulk simulant was characterised using the GSB BS1377 method of small pycnometer sieving (Hvorslev *et al.,* 1949) and depositing the sedimented material. The grain size fractions are 46.9 % sand (0.06-2.0 mm), 38.4 silt (3.9–62.5 µm) and 14.7 % clay (0.98–3.9 µm) (Figure 8).

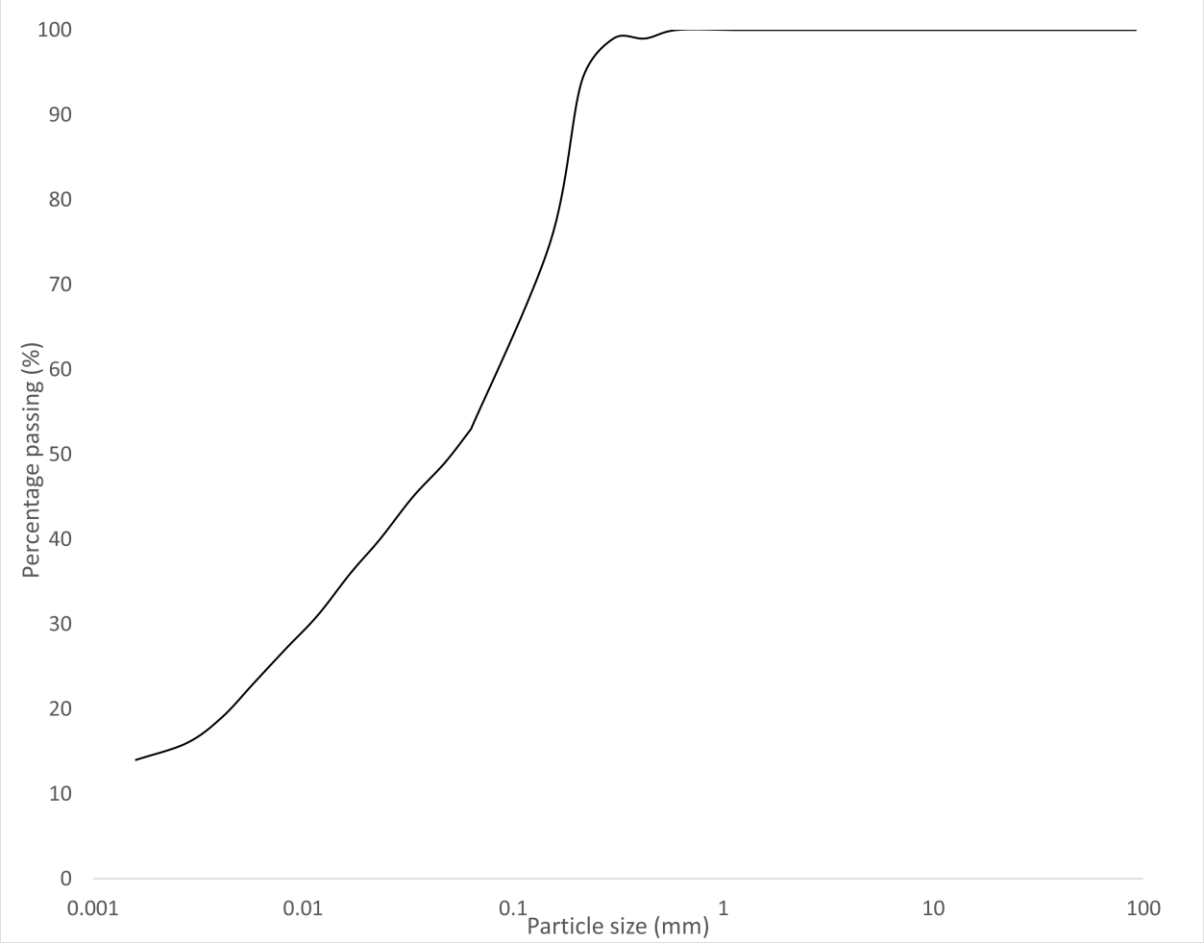

Figure 8: *Grain size distribution of the bulk simulant*

4.9 Optical microscopy

A Leica WILD MZ8 light microscope was used to image the bulk simulant (Figure 9). While the simulant was too fine to resolve the grain shape, expected grain shapes, based on the crystal structures of the minerals, are listed in Table S4 . Photographs of the simulant heaped and smoothed out are shown in Figure 10. These can be used in comparison to micro imager data from Mars such as Mars Hand Lens Imager (MAHLI) on *Curiosity* (Edgett *et al.* 2012) or at Oxia Planum from CLUPI (Josset *et al.* 2017), which may observe piles of drill tailings.

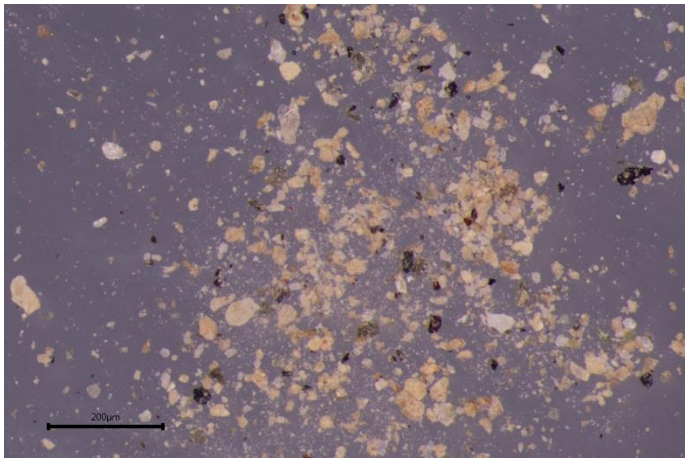

548

549 ***Figure 9:*** *Optical image of the simulant showing a range of grain shapes and sizes. A dark background is used to*
550 *show up light coloured minerals. Dark grains include biotite, pyroxene, Fe-silicate, red grains include siderite,*
551 *haematite and FeOOH while light grains dominate the simulant including vermiculite, orthoclase plagioclase,*
552 *serpentine.*
553

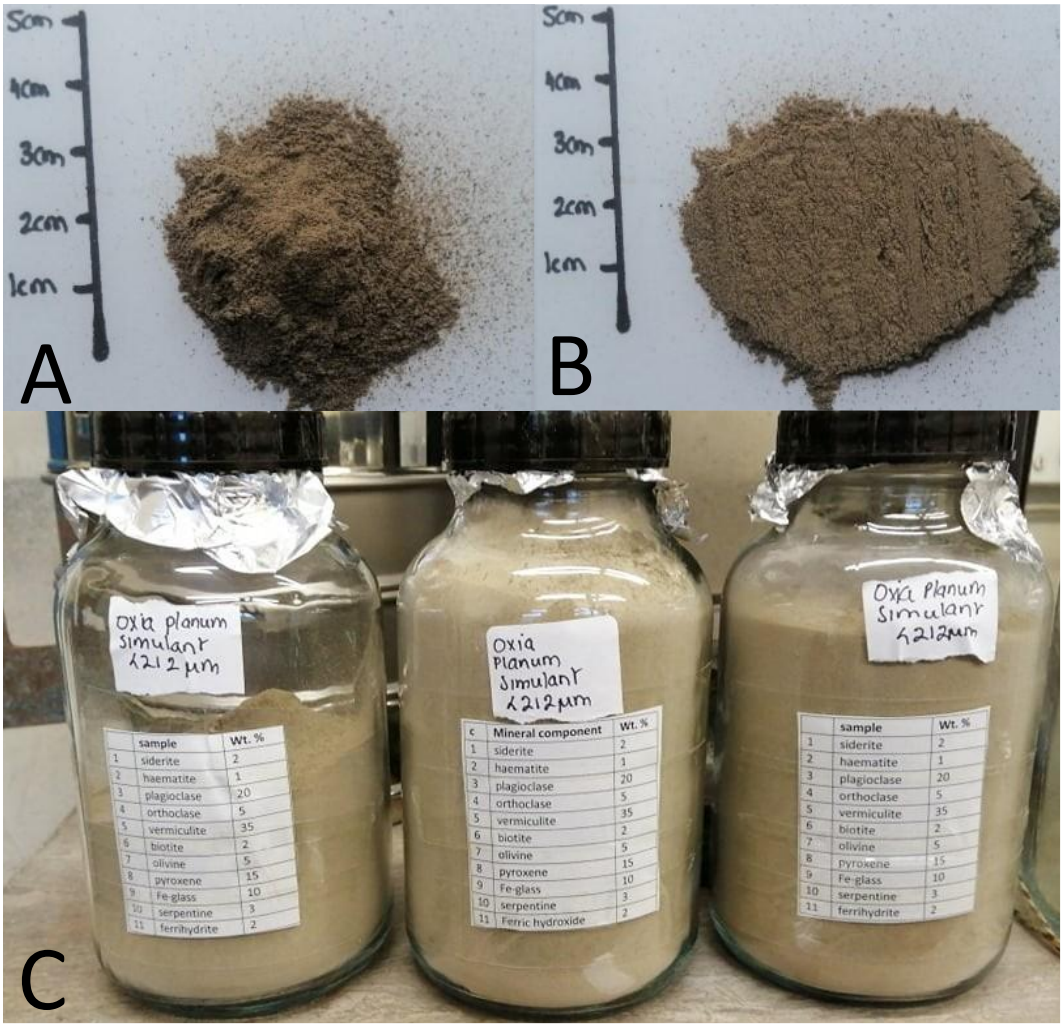

554

555 ***Figure 10:*** *Photos of bulk simulant: (A) piled simulant material; (B) simulant material when levelled out,*
556 *comparable with drill tailings or after being crossed with a sample flattening blade by the Rosalind Franklin rover;*
557 *(C) simulant storage at the Open University in glass jars with foil covered lids to prevent contamination.*

5 Discussion

The purpose of this study was to create a mineralogical simulant to represent the local mineralogy of Oxia Planum at a scale that is relevant to rover operations, which can then be used to facilitate analogue experimentation and support analysis of future rover data. The simulant design has been achieved by combining all the available remote sensing data with the most representative mineral assemblages identified from other rover exploration sites.

5.1 Simulant composition

5.1.1 Individual component analysis

SEM-EDS, EMPA and Raman spectroscopy were conducted to confirm the mineralogy and identify any accessory minerals present in the components, to ensure the bulk mineralogy of the final simulant reflected the abundances identified in Table 4.

SEM-EDS and EMPA analysis showed that test samples had more than one member of the same mineral group present. For example, pyroxene consisted of augite, pigeonite and omphacite, and plagioclase contained oligoclase and labradorite. In addition, the vermiculite sample contained Al-vermiculite in addition to Mg and Fe-vermiculite. However, the simulant design did not specify a member of the group, and the semi-quantitative data could be used to accommodate variations from the ideal composition. For some mineral components, accessory minerals were important contributors to the simulant; for example, orthoclase contained plagioclase (8 %) that was also required, and serpentine contained trace amounts of olivine (<1%). Negligible amounts of accessory minerals including hornblende, amphibole, Ca-silicate, calcite, macaulayite, bytownite and albite were also detected in components (Table 2). Accessory minerals are expected to total to <3 % of the simulant, so have no major effect on the overall mineralogy. Combining the simulant components in the amounts as proposed (Table 1) therefore results in an appropriate simulant mineralogy (Table 3).

5.1.2 Simulant Mineralogy

The simulant mineralogy was analysed using XRD, Near-IR spectroscopy and Mössbauer spectroscopy. Qualitative XRD from 3 aliquots of simulant shows the mineralogy of the simulant is homogenous with slight variations in peak intensities being accounted for by the crystal structures of the minerals.

Semi-quantitative analysis of these diffraction patterns was conducted by comparison to a constructed diffraction pattern based on the combined diffraction patterns of the components and the amounts that they were present in, using the FULLPAT software. This theoretical diffraction pattern is on good agreement with the simulant pattern suggesting the proportions in the simulant are as expected. Quantitative XRD was attempted using Rietveld refinement analysis and by analysis

of the amorphous material. These methods produced very variable results (Table S2). This was due to a range of issues: analysing mixtures of minerals can be difficult due to overlapping and broad reflections, poor availability of pure standards and variation in preferred orientation to name but a few (Bish and Chipera 1987). XRD analysis of phyllosilicates can be difficult because of similarities between their a and b unit cell dimensions; however, the c unit cell dimension differs between phyllosilicate minerals. Consequently, basal peaks (00l) are used as the primary method for phyllosilicate identification because these are the most defined (Moore and Reynolds 1997). In the case of a biotite and vermiculite mixture, the more defined peak for biotite leads to over or underrepresentation of the relative amounts of the two. This is also true in the case of the diffuse peaks for amorphous material where the inability to define a reliable identifying peak makes it difficult to quantify the material. While XRD is not onboard the *Rosalind Franklin* rover, the difficulty in quantifying the minerals in vermiculite-rich complex mixtures may be an issue for future missions.

Mössbauer analysis indicates that the Fe^{3+}/Fe_{total} ratio is 0.40, making the simulant dominated by Fe^{2+}, which does not correlate to enrichment in Fe^{3+} observed for much of the phyllosilicate terrain at Oxia Planum. However, the orbital data for Oxia Planum is not fully quantitative and many factors including dust cover and grain size could mean ground truths vary. In addition, controlling the Fe^{2+}/Fe^{3+} ratio was not one of the requirements of the simulant design. Future work could look at the variability of the Fe speciation, as was achieved by Ramkissoon *et al.* (2019) to create one or more modified simulant compositions.

Near-IR spectroscopy indicated the simulant has many similarities to the CRISM data, with absorption at 1.92 µm associated with the O-H stretch common to phyllosilicate minerals, in addition to absorption at 2.39 µm (Clark *et al.* 1990). Absorption at 2.32 µm is associated with the Fe,Mg-OH stretching and bending. However, the exact position depends on the Fe/Mg ratio and oxidation state of Fe (Clark *et al.* 1990; Mustard 1992; Chemtob *et al.* 2015; Michalski *et al.* 2015). Comparing to the Near-IR spectra for the components (Figure S1), the feature at 1.92 µm arises from the addition of vermiculite, siderite and serpentine. While the feature at 2.32 µm arises from olivine, serpentine, vermiculite and Fe-silicate.

5.1.3 Simulant Chemistry

Detailed geochemical analysis is difficult to obtain from orbit, therefore, this simulant is designed to represent a possible mineralogy at Oxia Planum and not a geochemistry. While this simulant is a mineralogical simulant and not a chemical simulant, the chemical composition was analysed using SEM-EDS and XRF and found to be dominated by SiO_2, MgO and FeO_T. Compared to the XRF data, the

calculated chemistry based on the SEM-EDS analysis of the components is as expected, with variations of <8 % for all compounds; this variation is accepted given that the mineralogy was the target.

Taylor *et al.* (2010) and Gasnault *et al.* (2010) used Mars Odyssey's gamma ray spectrometer (GRS) to identify geochemical provinces on Mars. Oxia Planum falls within a province extending from the southeast of Acidalia Planitia to the northwest of Arabia Terra and is shown to have elevated Ca and Fe content (Gasnault *et al.* 2010). Aside from the Al_2O_3 content, which is disproportionally high in the simulant (as discussed above), the highest variation in oxide percentage between the simulant and Sheepbed member is 3.32 wt. % (Table S5). The calculated CIA of the simulant was 51. A CIA above 40 indicates a weathered mineralogy. Values representative of an environment transitioning from a closed-system to an open-system occur at 50-55 on Mars (Nesbitt and Young 1982; McLennan *et al.* 2014). The simulant CIA value is likely to be skewed upwards by its high Al_2O_3 content. For comparison, it may be similar to the upper limit of the CIA values for Yellowknife Bay where CIA values between 35 and 45 correspond to closed system weathering (McLennan *et al.* 2014).

5.1.4 Simulant Physical Properties

The only constraint on the physical properties of this simulant was on the grain size used as it is designed to represent mineralogy, however, these are important to understand as they may influence the mechanical and thermal properties of future experiments. It should be noted that the simulant production method of crushing, milling and sieving the simulant to a specific grain size, is likely to have a large effect on its physical characteristics making then uncharacteristic of a natural sample. From the grain size distribution, the simulant is classified as a clay-silt-sand, which is consistent with the data from *Curiosity*; 53.1 % of the simulant falls within the silt-clay grain size, which is desirable for a phyllosilicate -bearing terrain (Table 9). The remainder is a fine to medium sand.

The bulk density of the simulant was found to be 1.15 g cm^{-3}. The bulk density of regolith at the Pathfinder lander site was estimated to be between 2–2.2 g cm^{-3} (Moore *et al.* 1999) and drift material at the Viking 1 landing site had an estimated bulk density of 1.15 ± 0.15 g cm^{-3} (Moore and Jakosky 1989), making the simulants bulk density on the lower side of what has been observed on Mars. This is likely to be owing to the low density of the phyllosilicate minerals that dominate the simulant. However, bulk density measurements for *in situ* phyllosilicate terrains on Mars have not yet been made, and there have been no estimates for the bulk density of the material at Oxia Planum. The porosity of the simulant was 61 %. The Viking missions' XRF suggested that porosity of the martian regolith was between 31 and 58% (Moore and Jakosky 1989). This is likely due to the clay-silt-sand particle distribution of the simulant.

5.2 Significance for rover exploration

5.2.1 Detectability of minerals at Oxia Planum

The development of this simulant highlights the potential difficulty in resolving individual mineral phases from assemblages. The Raman analysis shown here is useful for informing the analysis by the RLS instrument and is therefore relevant to the resolution of individual mineral phases. While phyllosilicate minerals can be identified with Raman and Near-IR spectrometry, determining lower weight percent minerals will be difficult without XRD. In addition, reactive Fe species give very broad peaks or no peaks. Moreover, the small particles sizes meant obtaining clear peaks with Raman spectroscopy was a challenge with a mixture comparable to a natural sample.

The Near-IR spectra for the simulant show some similarities to the CRISM and OMEGA data at Oxia Planum as illustrated in Figure 4 (Carter *et al.* 2016; Mandon *et al.* 2021; Brossier *et al.* 2022; Turner and Bridges 2017). These include absorption at 1.91 µm, associated with the presence of H_2O. While the absorption at ~2.3 µm is broader in the simulant than at Oxia Planum, suggesting the simulant Fe content is higher than at Oxia Planum (Mustard *et al.* 2008). In addition, differences in spectral slope can likely be accounted for by the powdered nature of the simulant as opposed to a consolidated rock at Oxia Planum (Harloff and Arnold 2001). These overall similarities would suggest that the SOPHIA simulant is a good match for Oxia Planum based on the spectral matches for the mineralogy from orbit. However, despite the increased spectral resolution compared to CRISM, no new features are resolved from the simulant spectra compared to the CRISM spectra, meaning additional instruments, such as the RLS, may be needed to fully assess the mineralogy *in situ.*

5.2.2 Relevance to biosignature preservation at Oxia Planum

As the simulant contains a plausible mineral assemblage for Oxia Planum, it represents a possible preservation environment for biosignatures. Consideration of the preservation potential of the simulant is therefore important. The simulant contains 35 % vermiculite, which would likely be the main preservation mineral at Oxia Planum. If the vermiculite is trioctahedral in nature it will likely have a higher propensity to preserve organic matter due to its higher Cation Exchange Charge (CEC) when compared to smectites (Jørgensen 1974; Krzesińska *et al.* 2021). The presence of Fe phases is also strongly linked to the preservation of organic molecules, with, over 20% of organic carbon on Earth being bound to reactive Fe mineral phases such as Fe (oxyhydr)oxides, which are closely associated with phyllosilicates (Lalonde *et al.* 2012). Up to 60% of the materials investigated in Gale crater are amorphous phases (Rampe *et al.* 2017, 2020). The Fe-rich endmember of these amorphous phases may represent reactive Fe (Bonsall *et al.* 2022). The presence of iron rich amorphous material has been shown to aid organic matter preservation (Lalonde *et al.* 2012), increasing the preservation potential of the simulant.

In addition, the entire mineral assemblage of the simulant is relevant to the modification of biomarker structures at Oxia Planum. Olivine and phyllosilicates have been shown to prevent biomarker degradation during impacts and UV degradation respectively (Parnell *et al.* 2005; Bowden *et al.* 2009; dos Santos *et al.* 2016; Montgomery *et al.* 2016; Furukawa *et al.* 2018). Both minerals have been detected at Oxia Planum and are included in the simulant, the quantities of which will affect overall biomarker preservation at Oxia Planum. This means experiments performed on the simulant will be specific to the mineralogy. If the mineralogy at Oxia Planum is like the simulant design, it is likely to have a high biomarker preservation potential.

5.2.3 Use in laboratory experiments

The SOPHIA simulant creates an opportunity for the community to perform a range of laboratory-based experiments specific to Oxia Planum. As this simulant is designed to represent a plausible *in situ* mineralogy at Oxia Planum, it is ideal for experimental studies investigating mineral interactions. These include possible mineral-microbe interactions and habitability studies (e.g., Cockell *et al.* 2005; Schuerger *et al.* 2012; Oliver *et al.* 2022). As the simulant represents the phyllosilicate terrains preserved from Noachian-aged terrains at Oxia Planum, it can also be used in biosignature formation, preservation, alteration and detectability studies specific to the payload on *Rosalind Franklin*. In addition, in the absence of chemical data for Oxia Planum, this simulant can be used as a baseline for the possible chemistry expected at Oxia Planum and used in geochemical investigations into rock-water interactions at the site, further constraining its alteration environment (Krzesinska *et al.* 2020; Krzesińska *et al.* 2021).

Conclusion and Summary

We have designed a new martian mineralogical simulant for Oxia Planum, SOPHIA (Simulant for Oxia Planum: Hydrated, Igneous, Amorphous), which is based on orbital data from Oxia Planum and geologically comparable sites on Mars. SOPHIA possesses a hypothesised mineral assemblage for Oxia Planum, which includes unaltered basaltic minerals, a phyllosilicate component and an amorphous component. The characterisation of the simulant performed here using Near-IR shows that SOPHIA is a good spectral match for Oxia Planum. This analysis, along with the Raman analysis, will assist in data interpretation from the rover's RLS, ISEM and MicrOmega instruments. SOPHIA can be used in a range of experiments concerning habitability and biomarker preservation, modification and detection in anticipation of the mission. The simulant may be available for use upon request depending on quantities required, the recipe and procedure described can also be modified for other experimental purposes.

Acknowledgments

The authors would like to thank Kay Knight and Michelle Higgins for sample preparation for the SEM-EDS and EMPA analysis , Matthew Kershaw for his assistance with XRD set up, Mark Fox-Powell for his role in acquiring the Near-IR spectra, and Rachael Hamp for her assistance in mineral sourcing. The anorthosite used here was provided by Andreas Børve Hovland, Norwegian Edelsplitt AS, and was mined from «Innstifjellet», Hellvik, Norway for no financial cost. Annie Lennox was the winner of the competition to name the simulant. SOPHIA is an acronym to describe the simulants composition, but also represents Sophia Brahe one of the first female astronomers. This work is funded by STFC (Grant No. ST/V50693X/1) and the Open University Strategic Research Area (Space), Research England Expanding Excellence in England (E3) fund (grant code 124.18) and preliminary work from an internship in 2019 funded by a Royal Astronomical Society bursary entitled 'The identification of geochemical biosignatures'. Additionally, the UK Space Agency are recognized for supporting P. Fawdon through grant ST/W002736/1 for science relating to *Rosalind Franklin* rover landing site characterisation activities, M. Patel through grants ST/V002295/1 and ST/V005332/1. C. Schröder acknowledges an appointment as Guest Investigator for the *Rosalind Franklin* rover mission by ESA supported by UK Space Agency grant ST/Y000072/1, and E. Bonsall and C. Schröder acknowledge STFC Training Grant ST/V50709X/1. The authors also wish to thank the CaSSIS spacecraft and instrument engineering teams. CaSSIS is a project of the University of Bern and funded through the Swiss Space Office via ESA's PRODEX program. The instrument hardware development was also supported by the Italian Space Agency (ASI) (ASI-INAF agreement no. I/2020-17-HH.0), INAF/Astronomical Observatory of Padova, and the Space Research Center (CBK) in Warsaw. Support from SGF (Budapest), the University of Arizona (Lunar and Planetary Lab.) and NASA are also gratefully acknowledged. Operations support from the UK Space Agency under grant ST/R003025/1 is also acknowledged.

References

Data is available at: 10.21954/ou.rd.22219903

Allen, C.C., Jager, K.M., Morris, R.V., Lindstrom, D.J., Lindtsrom, M.M. and Lockwood, J.P. 1998. Martian soil simulant available for scientific, educational study. *Eos, Transactions American Geophysical Union*, **79**, 405–409, https://doi.org/10.1029/98EO00309.

Apuzzo, A., Frigeri, A., Salvini, F., Brossier, J., Sanctis, M.C.D. and Schmidt, G.W. 2022. FRACTURED REGIONS OF EXOMARS 2022 LANDING SITE : MAPPING OF THE FRACTURED.

Baker, L.L. 2017. Basalt Weathering and the Volatile Budget of Early Mars. **2014**, 3081.

Bandfield, J.L. 2002. Global mineral distributions on Mars. *Journal of Geophysical Research: Planets*, **107**, 9-1-9–20, https://doi.org/10.1029/2001JE001510.

753 Banfield, J.F., Moreau, J.W., Chan, C.S., Welch, S.A. and Little, B. 2001. Mineralogical biosignatures and
754 the search for life on Mars. *Astrobiology*, **1**, 447–465,
755 https://doi.org/10.1089/153110701753593856.

756 Banin, A., Clark, B.C. and Waenke, H. 1992. *Surface Chemistry and Mineralogy.*

757 Bazylinski, D.A. and Moskowitz, B.M. 1997. Microbial biomineralization of magnetic iron minerals;
758 microbiology, magnetism and environmental significance. *Reviews in Mineralogy and*
759 *Geochemistry*, **35**, 181–223.

760 Beard, B.L., Johnson, C.M., Cox, L., Sun, H., Nealson, K.H. and Aguilar, C. 1999. Iron Isotope
761 Biosignatures. *Science*, **285**, 1889–1892, https://doi.org/10.1126/science.285.5435.1889.

762 Berlanga, G., Acosta-Maeda, T.E., et al. 2019. Remote Raman spectroscopy of natural rocks. *Applied*
763 *Optics*, **58**, 8971–8980, https://doi.org/10.1364/AO.58.008971.

764 Bibring, J.-P., Langevin, Y., et al. 2005. Mars Surface Diversity as Revealed by the OMEGA/Mars Express
765 Observations. *Science*, **307**, 1576–1581, https://doi.org/10.1126/science.1108806.

766 Bibring, J.-P., Langevin, Y., et al. 2006. Global Mineralogical and Aqueous Mars History Derived from
767 OMEGA/Mars Express Data. *Science*, **312**, 400–404,
768 https://doi.org/10.1126/science.1122659.

769 Bibring, J.-P., Hamm, V., Pilorget, C., Vago, J.L., and the MicrOmega Team. 2017. The MicrOmega
770 Investigation Onboard ExoMars. *Astrobiology*, **17**, 621–626,
771 https://doi.org/10.1089/ast.2016.1642.

772 Biroň, A., Sotak, J. and Bebej, J. 1999. Diagenetic trioctahedral phyllosilicates from sediments of the
773 Sambron Zone (Eastern Slovakia): XRD, SEM, and EMPA study. *Geologica Carpathica*, **50**, 257–
774 272.

775 Bish, D.L. and Chipera, S.J. 1987. Problems and Solutions in Quantitative Analysis of Complex Mixtures
776 by X-Ray Powder Diffraction. *Advances in X-Ray Analysis*, **31**, 295–308,
777 https://doi.org/10.1154/S0376030800022102.

778 Bishop, J.L. and Rampe, E.B. 2016. Evidence for a changing Martian climate from the mineralogy at
779 Mawrth Vallis. *Earth and Planetary Science Letters*, **448**, 42–48,
780 https://doi.org/10.1016/j.epsl.2016.04.031.

781 Bishop, J.L., Noe Dobrea, E.Z., et al. 2008. Phyllosilicate Diversity and Past Aqueous Activity Revealed
782 at Mawrth Vallis, Mars. *Science (New York, N.Y.)*, **321**, 830–833,
783 https://doi.org/10.1126/science.1159699.

784 Bishop, J.L., Gross, C., et al. 2020. Multiple mineral horizons in layered outcrops at Mawrth Vallis, Mars,
785 signify changing geochemical environments on early Mars. *Icarus*, **341**, 113634,
786 https://doi.org/10.1016/j.icarus.2020.113634.

787 Boettger, U., de Vera, J.-P., Fritz, J., Weber, I., Hübers, H.-W. and Schulze-Makuch, D. 2012. Optimizing
788 the detection of carotene in cyanobacteria in a martian regolith analogue with a Raman
789 spectrometer for the ExoMars mission. *Planetary and Space Science*, **60**, 356–362,
790 https://doi.org/10.1016/j.pss.2011.10.017.

Bonsall, E., McHugh, M., Lerman, H., Hutchinson, I. and Schröder, C. 2022. Reactive Iron Mineral Phases May Preserve Organic Carbon on Mars: Implications for Raman Spectroscopy. **2678**, 2148.

Bowden, S.A., Parnell, J. and Burchell, M.J. 2009. Survival of organic compounds in ejecta from hypervelocity impacts on ice. *International Journal of Astrobiology*, **8**, 19–25, https://doi.org/10.1017/S147355040900442X.

Bowen, A.P., Bridges, J., et al. 2022. A CaSSIS and HiRISE map of the Clay-bearing Unit at the ExoMars 2022 landing site in Oxia Planum. *Planetary and Space Science*, **214**, 105429, https://doi.org/10.1016/j.pss.2022.105429.

Bridges, J.C. and Warren, P.H. 2006. The SNC meteorites: basaltic igneous processes on Mars. *Journal of the Geological Society*, **163**, 229–251, https://doi.org/10.1144/0016-764904-501.

Brindley, G.W. 1983. CLAYS, CLAY MINERALSClays, clay minerals. *In*: *Mineralogy*. Encyclopedia of Earth Science, 69–80., https://doi.org/10.1007/0-387-30720-6_23.

Bristow, T.F., Rampe, E.B., et al. 2018. Clay mineral diversity and abundance in sedimentary rocks of Gale crater, Mars. *Science Advances*, **4**, eaar3330, https://doi.org/10.1126/sciadv.aar3330.

Brossier, J., Altieri, F., et al. 2022. Constraining the spectral behavior of the clay-bearing outcrops in Oxia Planum, the landing site for ExoMars “Rosalind Franklin” rover. *Icarus*, **386**, 115114, https://doi.org/10.1016/j.icarus.2022.115114.

Broz, A.P. 2020. Organic Matter Preservation in Ancient Soils of Earth and Mars. *Life*, **10**, 113, https://doi.org/10.3390/life10070113.

Bultel, B., Viennet, J.-C., Poulet, F., Carter, J. and Werner, S.C. 2019. Detection of Carbonates in Martian Weathering Profiles. *Journal of Geophysical Research: Planets*, **124**, 989–1007, https://doi.org/10.1029/2018JE005845.

Campos, M. and Int, -M. n.d. Applications of quartering method in soils and foods.

Cannon, K.M., Britt, D.T., Smith, T.M., Fritsche, R.F. and Batcheldor, D. 2019. Mars global simulant MGS-1: A Rocknest-based open standard for basaltic martian regolith simulants. *Icarus*, **317**, 470–478, https://doi.org/10.1016/j.icarus.2018.08.019.

Carter, J., Poulet, F., Bibring, J.-P. and Murchie, S. 2010. Detection of Hydrated Silicates in Crustal Outcrops in the Northern Plains of Mars. *Science*, **328**, 1682–1686.

Carter, J., Poulet, F., Bibring, J.-P., Mangold, N. and Murchie, S. 2013. Hydrous minerals on Mars as seen by the CRISM and OMEGA imaging spectrometers: Updated global view. *Journal of Geophysical Research: Planets*, **118**, 831–858, https://doi.org/10.1029/2012JE004145.

Carter, J., Quantin, C., et al. 2016. OXIA PLANUM, A CLAY-LADEN LANDING SITE PROPOSED FOR THE EXOMARS ROVER MISSION: AQUEOUS MINERALOGY AND ALTERATION SCENARIOS. 2.

Caswell, T.E. and Milliken, R.E. 2017. Evidence for hydraulic fracturing at Gale crater, Mars: Implications for burial depth of the Yellowknife Bay formation. *Earth and Planetary Science Letters*, **468**, 72–84, https://doi.org/10.1016/j.epsl.2017.03.033.

Chemtob, S.M., Nickerson, R.D., Morris, R.V., Agresti, D.G. and Catalano, J.G. 2015. Synthesis and structural characterization of ferrous trioctahedral smectites: Implications for clay mineral genesis and detectability on Mars. *Journal of Geophysical Research: Planets*, **120**, 1119–1140, https://doi.org/10.1002/2014JE004763.

Chipera, S.J. and Bish, D.L. 2002. ıt FULLPAT: a full-pattern quantitative analysis program for X-ray powder diffraction using measured and calculated patterns. *Journal of Applied Crystallography*, **35**, 744–749, https://doi.org/10.1107/S0021889802017405.

Clark, J., Sutter, B., et al. 2021. A Review of Sample Analysis at Mars-Evolved Gas Analysis Laboratory Analog Work Supporting the Presence of Perchlorates and Chlorates in Gale Crater, Mars. *Minerals*, **11**, 475, https://doi.org/10.3390/min11050475.

Clark, R.N., King, T.V.V., Klejwa, M., Swayze, G.A. and Vergo, N. 1990. High spectral resolution reflectance spectroscopy of minerals. *Journal of Geophysical Research: Solid Earth*, **95**, 12653–12680, https://doi.org/10.1029/JB095iB08p12653.

Clifford, S.M. and Parker, T.J. 2001. The Evolution of the Martian Hydrosphere: Implications for the Fate of a Primordial Ocean and the Current State of the Northern Plains. *Icarus*, **154**, 40–79, https://doi.org/10.1006/icar.2001.6671.

Coates, A.J., Jaumann, R., et al. 2017. The PanCam Instrument for the ExoMars Rover. *Astrobiology*, **17**, 511–541, https://doi.org/10.1089/ast.2016.1548.

Cockell, C.S., Schuerger, A.C., Billi, D., Friedmann, E.I. and Panitz, C. 2005. Effects of a Simulated Martian UV Flux on the Cyanobacterium, Chroococcidiopsis sp. 029. *Astrobiology*, **5**, 127–140, https://doi.org/10.1089/ast.2005.5.127.

Cousins, C.R., Gunn, M., et al. 2012. Selecting the geology filter wavelengths for the ExoMars Panoramic Camera instrument. *Planetary and Space Science*, **1**, 80–100, https://doi.org/10.1016/j.pss.2012.07.009.

Dartnell, L.R., Desorgher, L., Ward, J.M. and Coates, A.J. 2007. Modelling the surface and subsurface Martian radiation environment: Implications for astrobiology. *Geophysical Research Letters*, **34**, https://doi.org/10.1029/2006GL027494.

Dartnell, L.R., Page, K., et al. 2012. Destruction of Raman biosignatures by ionising radiation and the implications for life detection on Mars. *Analytical and Bioanalytical Chemistry*, **403**, 131–144, https://doi.org/10.1007/s00216-012-5829-6.

De Sanctis, M.C., Altieri, F., et al. 2022. Exploring the Shallow Subsurface of Mars with the Ma_MISS Spectrometer on the ExoMars Rover Rosalind Franklin. *The Planetary Science Journal*, **3**, 142, https://doi.org/10.3847/PSJ/ac694f.

Dehouck, E., Carter, J., et al. n.d. Curiosity's traverse through the upper Murray formation (Gale crater): ground truth for orbital detections of Martian clay minerals. 1.

Dickeson, Z.I. and Davis, J.M. 2020. Martian oceans. *Astronomy & Geophysics*, **61**, 3.11-3.17, https://doi.org/10.1093/astrogeo/ataa038.

dos Santos, R., Patel, M., Cuadros, J. and Martins, Z. 2016. Influence of mineralogy on the preservation of amino acids under simulated Mars conditions. *Icarus*, **277**, 342–353, https://doi.org/10.1016/j.icarus.2016.05.029.

868 Edgett, K.S., Yingst, R.A., et al. 2012. Curiosity's Mars Hand Lens Imager (MAHLI) Investigation. *Space*
869 *Science Reviews*, **170**, 259–317, https://doi.org/10.1007/s11214-012-9910-4.

870 Ehlmann, B.L. and Edwards, C.S. 2014. Mineralogy of the Martian Surface. *Annual Review of Earth and*
871 *Planetary Sciences*, **42**, 291–315, https://doi.org/10.1146/annurev-earth-060313-055024.

872 Ehlmann, B.L., Mustard, J.F., et al. 2008. Orbital Identification of Carbonate-Bearing Rocks on Mars.
873 *Science*, **322**, 1828–1832, https://doi.org/10.1126/science.1164759.

874 Ehlmann, B.L., Mustard, J.F., Murchie, S.L., Bibring, J.-P., Meunier, A., Fraeman, A.A. and Langevin, Y.
875 2011. Subsurface water and clay mineral formation during the early history of Mars. *Nature*,
876 **479**, 53–60, https://doi.org/10.1038/nature10582.

877 Ertem, G., Ertem, M.C., McKay, C.P. and Hazen, R.M. 2017. Shielding biomolecules from effects of
878 radiation by Mars analogue minerals and soils. *International Journal of Astrobiology*, **16**, 280–
879 285, https://doi.org/10.1017/S1473550416000331.

880 Fawdon, P., Grindrod, P., et al. 2021. The geography of Oxia Planum. *Journal of Maps*, **17**, 621–637,
881 https://doi.org/10.1080/17445647.2021.1982035.

882 Fawdon, P., Balme, M., Davis, J., Bridges, J., Gupta, S. and Quantin-Nataf, C. 2022. Rivers and Lakes in
883 Western Arabia Terra: The Fluvial Catchment of the ExoMars 2022 Rover Landing Site. *Journal*
884 *of Geophysical Research: Planets*, **127**, e2021JE007045,
885 https://doi.org/10.1029/2021JE007045.

886 Fawdon, P., Orgel, C., et al. 2023. The HiRISE Scale Map of the Proposed Landing Site for the ExoMars
887 Rosalind Franklin Rover in Oxia Planum. *In*: 54rd Lunar and Planetary Science Conference.
888 Abstract #2037.

889 Fitzpatrick, E.A. 1984. Principles of thin section preparation. *In*: Fitzpatrick, E. A. (ed.)
890 *Micromorphology of Soils*. 1–5., https://doi.org/10.1007/978-94-009-5544-8_1.

891 Foley, C.N., Economou, T.E., Clayton, R.N. and Dietrich, W. 2003. Calibration of the Mars Pathfinder
892 alpha proton X-ray spectrometer. *Journal of Geophysical Research: Planets*, **108**,
893 https://doi.org/10.1029/2002JE002018.

894 Fraser, D.G., Fitz, D., Jakschitz, T. and Rode, B.M. 2011. Selective adsorption and chiral amplification
895 of amino acids in vermiculite clay-implications for the origin of biochirality. *Physical chemistry*
896 *chemical physics: PCCP*, **13**, 831–838, https://doi.org/10.1039/c0cp01388a.

897 Furukawa, Y., Takase, A., Sekine, T., Kakegawa, T. and Kobayashi, T. 2018. Racemization of Valine by
898 Impact-Induced Heating. *Origins of Life and Evolution of Biospheres*, **48**, 131–139,
899 https://doi.org/10.1007/s11084-017-9539-0.

900 García-Ruiz, J.M., Hyde, S.T., Carnerup, A.M., Christy, A.G., Van Kranendonk, M.J. and Welham, N.J.
901 2003. Self-Assembled Silica-Carbonate Structures and Detection of Ancient Microfossils.
902 *Science*, **302**, 1194–1197, https://doi.org/10.1126/science.1090163.

903 Gary-Bicas, C.E. and Rogers, A.D. 2021. Geologic and Thermal Characterization of Oxia Planum Using
904 Mars Odyssey THEMIS Data. *Journal of Geophysical Research: Planets*, **126**, e2020JE006678,
905 https://doi.org/10.1029/2020JE006678.

906 Gasnault, O., Jeffrey Taylor, G., et al. 2010. Quantitative geochemical mapping of martian elemental
907 provinces. *Icarus*, **207**, 226–247, https://doi.org/10.1016/j.icarus.2009.11.010.

908 Gellert, R., Rieder, R., et al. 2006. Alpha Particle X-Ray Spectrometer (APXS): Results from Gusev crater
909 and calibration report. *Journal of Geophysical Research: Planets*, **111**,
910 https://doi.org/10.1029/2005JE002555.

911 Georgiou, C.D. and Deamer, D.W. 2014. Lipids as Universal Biomarkers of Extraterrestrial Life.
912 *Astrobiology*, **14**, 541–549, https://doi.org/10.1089/ast.2013.1134.

913 Glavin, D.P., Freissinet, C., et al. 2013. Evidence for perchlorates and the origin of chlorinated
914 hydrocarbons detected by SAM at the Rocknest aeolian deposit in Gale Crater. *Journal of*
915 *Geophysical Research: Planets*, **118**, 1955–1973, https://doi.org/10.1002/jgre.20144.

916 Goesmann, F., Brinckerhoff, W.B., et al. 2017. The Mars Organic Molecule Analyzer (MOMA)
917 Instrument: Characterization of Organic Material in Martian Sediments. *Astrobiology*, **17**,
918 655–685, https://doi.org/10.1089/ast.2016.1551.

919 Grotzinger, J.P. 2014. Habitability, Taphonomy, and the Search for Organic Carbon on Mars. *Science*,
920 **343**, 386–387, https://doi.org/10.1126/science.1249944.

921 Harloff, J. and Arnold, G. 2001. Near-infrared reflectance spectroscopy of bulk analog materials for
922 planetary crust. *Planetary and Space Science*, **49**, 191–211, https://doi.org/10.1016/S0032-
923 0633(00)00132-X.

924 Harris, J.K., Cousins, C.R., et al. 2015. Remote detection of past habitability at Mars-analogue
925 hydrothermal alteration terrains using an ExoMars Panoramic Camera emulator. *Icarus*, **252**,
926 284–300, https://doi.org/10.1016/j.icarus.2015.02.004.

927 He, Y., Buch, A., et al. 2020. Influence of Calcium Perchlorate on the Search for Organics on Mars with
928 Tetramethylammonium Hydroxide Thermochemolysis. *Astrobiology*, **21**, 279–297,
929 https://doi.org/10.1089/ast.2020.2252.

930 Head III, J.W., Kreslavsky, M., et al. 1998. Oceans in the past history of Mars: Tests for their presence
931 using Mars Orbiter Laser Altimeter (MOLA) data. *Geophysical Research Letters*, **25**, 4401–
932 4404, https://doi.org/10.1029/1998GL900116.

933 Hecht, M.H., Kounaves, S.P., et al. 2009. Detection of Perchlorate and the Soluble Chemistry of Martian
934 Soil at the Phoenix Lander Site. *Science*, **325**, 64–67,
935 https://doi.org/10.1126/science.1172466.

936 Hedges, J.I. 1977. The association of organic molecules with clay minerals in aqueous solutions.
937 *Geochimica et Cosmochimica Acta*, **41**, 1119–1123, https://doi.org/10.1016/0016-
938 7037(77)90106-5.

939 Hvorslev, M.J. //. SUBSURFACE EXPLORATION AND SAMPLING OF SOILS FOR CIVIL ENGINEERING
940 PURPOSES.

941 Hynek, B.M., Beach, M. and Hoke, M.R.T. 2010. Updated global map of Martian valley networks and
942 implications for climate and hydrologic processes. *Journal of Geophysical Research: Planets*,
943 **115**, https://doi.org/10.1029/2009JE003548.

I, K., DobrolenskyYurii, et al. 2017. Infrared Spectrometer for ExoMars: A Mast-Mounted Instrument for the Rover. *Astrobiology*, https://doi.org/10.1089/ast.2016.1543.

Ivanov, M.A. and Head, J.W. 2001. Chryse Planitia, Mars: Topographic configuration, outflow channel continuity and sequence, and tests for hypothesized ancient bodies of water using Mars Orbiter Laser Altimeter (MOLA) data. *Journal of Geophysical Research: Planets*, **106**, 3275–3295, https://doi.org/10.1029/2000JE001257.

Jørgensen, P. 1974. C.E. Weaver L.D. Pollard The Chemistry of Clay Minerals Developments in Sedimentology 15 1973 Elsevier Amsterdam 213 Dfl. 65.00. *Engineering Geology*, **8**, 401–402, https://doi.org/10.1016/0013-7952(74)90030-1.

Josset, J.-L., Westall, F., et al. 2017. The Close-Up Imager Onboard the ESA ExoMars Rover: Objectives, Description, Operations, and Science Validation Activities. *Astrobiology*, **17**, 595–611, https://doi.org/10.1089/ast.2016.1546.

J.-P, B., Soufflot, A., et al. 2004. OMEGA : Observatoire pour la Minéralogie, l'Eau, les Glaces et l'Activité.

K4 Soils testing laboratory, Watford, UK. n.d. K4 Soils Testing Laboratory. *K4 Soils Laboratory*https://k4soils.com/.

King, T.V.V. and Ridley, W.I. 1987. Relation of the spectroscopic reflectance of olivine to mineral chemistry and some remote sensing implications. *Journal of Geophysical Research: Solid Earth*, **92**, 11457–11469, https://doi.org/10.1029/JB092iB11p11457.

Klingelhoefer, G., Morris, R.V., deSouza, P.A. and Bernhardt, B. 2003. The Miniaturized Moessbauer Spectrometer MIMOS II of the Athena Payload for the 2003 MER Missions.

Klingelhöfer, G., Morris, R.V., et al. 2004. Jarosite and Hematite at Meridiani Planum from Opportunity's Mössbauer Spectrometer. *Science*, **306**, 1740–1745, https://doi.org/10.1126/science.1104653.

Kminek, G. and Bada, J.L. 2006. The effect of ionizing radiation on the preservation of amino acids on Mars. *Earth and Planetary Science Letters*, **245**, 1–5, https://doi.org/10.1016/j.epsl.2006.03.008.

Krzesinska, A., Bultel, B., Viennet, J.-C., Loizeau, D. and Werner, S. 2020. *Experimental Approach to Understand Mineralogy and Aqueous Alteration History of Oxia Planum, ExoMars 2020 Landing Site*. **EGU2020-10649**, https://doi.org/10.5194/egusphere-egu2020-10649.

Krzesińska, A.M., Bultel, B., Loizeau, D., Craw, D., April, R., Poulet, F. and Werner, S.C. 2021. Mineralogical and Spectral (Near-Infrared) Characterization of Fe-Rich Vermiculite-Bearing Terrestrial Deposits and Constraints for Mineralogy of Oxia Planum, ExoMars 2022 Landing Site. *Astrobiology*, **21**, 997–1016, https://doi.org/10.1089/ast.2020.2410.

Lafuente, B., Downs, R.T., Yang, H. and Stone, N. 2015. 1. The power of databases: The RRUFF project. *In*: *1. The Power of Databases: The RRUFF Project*. 1–30., https://doi.org/10.1515/9783110417104-003.

Lai, J.C., Horgan, B., Bell III, J.F. and Wellington, D.F. 2019. Assessing martian bedrock mineralogy through "windows" in the dust using near-infrared and thermal infrared remote sensing. *Icarus*, **324**, 15–40, https://doi.org/10.1016/j.icarus.2019.01.019.

Lalonde, K., Mucci, A., Ouellet, A. and Gélinas, Y. 2012. Preservation of organic matter in sediments promoted by iron. *Nature*, **483**, 198–200, https://doi.org/10.1038/nature10855.

Leask, E.K., Ehlmann, B.L., Dundar, M.M., Murchie, S.L. and Seelos, F.P. 2018. Challenges in the Search for Perchlorate and Other Hydrated Minerals With 2.1-µm Absorptions on Mars. *Geophysical Research Letters*, **45**, 12,180-12,189, https://doi.org/10.1029/2018GL080077.

Lin, C.Y., Turchyn, A.V., Krylov, A. and Antler, G. 2020. The microbially driven formation of siderite in salt marsh sediments. *Geobiology*, **18**, 207–224, https://doi.org/10.1111/gbi.12371.

Liu, J., Michalski, J.R., Tan, W., He, H., Ye, B. and Xiao, L. 2021. Anoxic chemical weathering under a reducing greenhouse on early Mars. *Nature Astronomy*, **5**, 503–509, https://doi.org/10.1038/s41550-021-01303-5.

Loizeau, D., Mangold, N., Poulet, F., Bibring, J.-P., Bishop, J.L., Michalski, J. and Quantin, C. 2015. History of the clay-rich unit at Mawrth Vallis, Mars: High-resolution mapping of a candidate landing site. *Journal of Geophysical Research (Planets)*, **120**, 1820–1846, https://doi.org/10.1002/2015JE004894.

Lowe, D.R., Bishop, J.L., Loizeau, D., Wray, J.J. and Beyer, R.A. 2020. Deposition of >3.7 Ga clay-rich strata of the Mawrth Vallis Group, Mars, in lacustrine, alluvial, and aeolian environments. *GSA Bulletin*, **132**, 17–30, https://doi.org/10.1130/B35185.1.

Mandon, L., Parkes Bowen, A., et al. 2021. Morphological and Spectral Diversity of the Clay-Bearing Unit at the ExoMars Landing Site Oxia Planum. *Astrobiology*, **21**, 464–480, https://doi.org/10.1089/ast.2020.2292.

McKeown, N.K., Bishop, J.L., et al. 2009. Characterization of phyllosilicates observed in the central Mawrth Vallis region, Mars, their potential formational processes, and implications for past climate. *Journal of Geophysical Research: Planets*, **114**, https://doi.org/10.1029/2008JE003301.

McLennan, S.M., Anderson, R.B., et al. 2014. Elemental Geochemistry of Sedimentary Rocks at Yellowknife Bay, Gale Crater, Mars. *Science*, **343**, https://doi.org/10.1126/science.1244734.

Michalski, J., Jean-PierreBibring, et al. 2010. The Mawrth Vallis Region of Mars: A Potential Landing Site for the Mars Science Laboratory (MSL) Mission. *Astrobiology*, **10**, 687–703, https://doi.org/10.1089/ast.2010.0491.

Michalski, J.R., Cuadros, J., Bishop, J.L., Darby Dyar, M., Dekov, V. and Fiore, S. 2015. Constraints on the crystal-chemistry of Fe/Mg-rich smectitic clays on Mars and links to global alteration trends. *Earth and Planetary Science Letters*, **427**, 215–225, https://doi.org/10.1016/j.epsl.2015.06.020.

Milam, K.A., McSween, H.Y., Moersch, J. and Christensen, P.R. 2010. Distribution and variation of plagioclase compositions on Mars. *Journal of Geophysical Research: Planets*, **115**, https://doi.org/10.1029/2009JE003495.

Millan, M., Szopa, C., Buch, A., Summons, R.E., Navarro-Gonzalez, R., Mahaffy, P.R. and Johnson, S.S. 2020. Influence of Calcium Perchlorate on Organics Under SAM-Like Pyrolysis Conditions: Constraints on the Nature of Martian Organics. *Journal of Geophysical Research: Planets*, **125**, e2019JE006359, https://doi.org/10.1029/2019JE006359.

1024 Molina, A., López, I., Prieto-Ballesteros, O., Fernández-Remolar, D., de Pablo, M.Á. and Gómez, F. 2017.
1025 Coogoon Valles, western Arabia Terra: Hydrological evolution of a complex Martian channel
1026 system. *Icarus*, **293**, 27–44, https://doi.org/10.1016/j.icarus.2017.04.002.

1027 Montgomery, W., Bromiley, G.D. and Sephton, M.A. 2016. The nature of organic records in impact
1028 excavated rocks on Mars. *Scientific Reports*, **6**, 30947, https://doi.org/10.1038/srep30947.

1029 Moore, H.J. and Jakosky, B.M. 1989. Viking landing sites, remote-sensing observations, and physical
1030 properties of Martian surface materials. *Icarus*, **81**, 164–184, https://doi.org/10.1016/0019-
1031 1035(89)90132-2.

1032 Moore, H.J., Bickler, D.B., et al. 1999. Soil-like deposits observed by Sojourner, the Pathfinder rover.
1033 *Journal of Geophysical Research: Planets*, **104**, 8729–8746,
1034 https://doi.org/10.1029/1998JE900005.

1035 Moreras-Marti, A., Fox-Powell, M., Cousins, C.R., Macey, M.C. and Zerkle, A.L. 2022. Sulfur isotopes as
1036 biosignatures for Mars and Europa exploration. *Journal of the Geological Society*, jgs2021-134,
1037 https://doi.org/10.1144/jgs2021-134.

1038 Morris, R.V., Schröder, C., Klingelhöfer, G. and Agresti, D.G. 2019. *Mössbauer Spectroscopy at Gusev*
1039 *Crater and Meridiani Planum: Iron Mineralogy, Oxidation State, and Alteration on Mars*,
1040 https://doi.org/10.1017/9781316888872.029.

1041 Mustard, J.F. 1992. Chemical analysis of actinolite from reflectance spectra. *American Mineralogist*,
1042 **77**, 345–358.

1043 Mustard, J.F. 2005. Olivine and Pyroxene Diversity in the Crust of Mars. *Science*, **307**, 1594–1597,
1044 https://doi.org/10.1126/science.1109098.

1045 Mustard, J.F., Murchie, S.L., et al. 2008. Hydrated silicate minerals on Mars observed by the Mars
1046 Reconnaissance Orbiter CRISM instrument. *Nature*, **454**, 305–309,
1047 https://doi.org/10.1038/nature07097.

1048 Nesbitt, H.W. and Young, G.M. 1982. Early Proterozoic climates and plate motions inferred from major
1049 element chemistry of lutites. *Nature (London)*, **299**, 715–717,
1050 https://doi.org/10.1038/299715a0.

1051 Noe Dobrea, E.Z.N., Bishop, J.L., et al. 2010. Mineralogy and stratigraphy of phyllosilicate-bearing and
1052 dark mantling units in the greater Mawrth Vallis/west Arabia Terra area: Constraints on
1053 geological origin. *Journal of Geophysical Research: Planets*, **115**,
1054 https://doi.org/10.1029/2009JE003351.

1055 Noe Dobrea, E.Z.N., Michalski, J. and Swayze, G. 2011. Aqueous mineralogy and stratigraphy at and
1056 around the proposed Mawrth Vallis MSL Landing Site: New insights into the aqueous history
1057 of the region.

1058 Noffke, N., Gerdes, G., Klenke, T. and Krumbein, W.E. 2001. Microbially Induced Sedimentary
1059 Structures: A New Category within the Classification of Primary Sedimentary Structures.
1060 *Journal of Sedimentary Research*, **71**, 649–656, https://doi.org/10.1306/2DC4095D-0E47-
1061 11D7-8643000102C1865D.

1062 Noffke, N., Christian, D., Wacey, D. and Hazen, R.M. 2013. Microbially Induced Sedimentary Structures
1063 Recording an Ancient Ecosystem in the *ca.* 3.48 Billion-Year-Old Dresser Formation, Pilbara,
1064 Western Australia. *Astrobiology*, **13**, 1103–1124, https://doi.org/10.1089/ast.2013.1030.

1065 Ody, A., Poulet, F., Bibring, J.-P., Loizeau, D., Carter, J., Gondet, B. and Langevin, Y. 2013. Global
1066 investigation of olivine on Mars: Insights into crust and mantle compositions. *Journal of*
1067 *Geophysical Research: Planets*, **118**, 234–262, https://doi.org/10.1029/2012JE004149.

1068 Oliver, J.A.W., Kelbrick, M., et al. 2022. Sulfur Cycling as a Viable Metabolism under Simulated
1069 Noachian/Hesperian Chemistries. *Life*, **12**, 523, https://doi.org/10.3390/life12040523.

1070 Osterloo, et al., 2008. n.d. Chloride-Bearing Materials in the Southern Highlands of Mars.

1071 Pan, L., Carter, J., et al. 2021. Voluminous Silica Precipitated from Martian Waters during Late-stage
1072 Aqueous Alteration. *The Planetary Science Journal*, **2**, 65,
1073 https://doi.org/10.3847/PSJ/abe541.

1074 Parker, T.J., Stephen Saunders, R. and Schneeberger, D.M. 1989. Transitional morphology in West
1075 Deuteronilus Mensae, Mars: Implications for modification of the lowland/upland boundary.
1076 *Icarus*, **82**, 111–145, https://doi.org/10.1016/0019-1035(89)90027-4.

1077 Parker, T.J., Gorsline, D.S., Saunders, R.S., Pieri, D.C. and Schneeberger, D.M. 1993. Coastal
1078 geomorphology of the Martian northern plains. *Journal of Geophysical Research: Planets*, **98**,
1079 11061–11078, https://doi.org/10.1029/93JE00618.

1080 Parkes Bowen, A., Mandon, L., et al. 2020. Using band ratioed CaSSIS imagery and analysis of fracture
1081 morphology to characterise Oxia Planum's clay-bearing unit. EPSC2020-877,
1082 https://doi.org/10.5194/epsc2020-877.

1083 Parnell, J., Osinski, G.R., Lee, P., Green, P.F. and Baron, M.J. 2005. Thermal alteration of organic matter
1084 in an impact crater and the duration of postimpact heating. *Geology*, **33**, 373,
1085 https://doi.org/10.1130/G21204.1.

1086 Parnell, J., Cullen, D., et al. 2007. Searching for Life on Mars: Selection of Molecular Targets for ESA's
1087 Aurora ExoMars Mission. *Astrobiology*, **7**, 578–604, https://doi.org/10.1089/ast.2006.0110.

1088 Peters, G.H., Abbey, W., et al. 2008. Mojave Mars simulant—Characterization of a new geologic Mars
1089 analog. *Icarus*, **197**, 470–479, https://doi.org/10.1016/j.icarus.2008.05.004.

1090 Poch, O., Jaber, M., et al. 2015. Effect of Nontronite Smectite Clay on the Chemical Evolution of Several
1091 Organic Molecules under Simulated Martian Surface Ultraviolet Radiation Conditions.
1092 *Astrobiology*, **15**, 221–237, https://doi.org/10.1089/ast.2014.1230.

1093 Poulet, F., Gross, C., Horgan, B., Loizeau, D., Bishop, J.L., Carter, J. and Orgel, C. 2020. Mawrth Vallis,
1094 Mars: A Fascinating Place for Future *In Situ* Exploration. *Astrobiology*, **20**, 199–234,
1095 https://doi.org/10.1089/ast.2019.2074.

1096 Quantin-Nataf, C., Carter, J., et al. 2021. Oxia Planum: The Landing Site for the ExoMars "Rosalind
1097 Franklin" Rover Mission: Geological Context and Prelanding Interpretation. *Astrobiology*,
1098 https://doi.org/10.1089/ast.2019.2191.

1099 Ramkissoon, N.K., Pearson, V.K., et al. 2019. New simulants for martian regolith: Controlling iron
1100 variability. *Planetary and Space Science*, **179**, 104722,
1101 https://doi.org/10.1016/j.pss.2019.104722.

1102 Rampe, E.B., Blake, D.F., et al. 2020. Mineralogy and geochemistry of sedimentary rocks and eolian
1103 sediments in Gale crater, Mars: A review after six Earth years of exploration with Curiosity.
1104 *Geochemistry*, **80**, 125605, https://doi.org/10.1016/j.chemer.2020.125605.

1105 Rancourt, D.G. and Ping, J.Y. 1991. Voigt-based methods for arbitrary-shape static hyperfine
1106 parameter distributions in Mössbauer spectroscopy. *Nuclear Instruments and Methods in*
1107 *Physics Research Section B: Beam Interactions with Materials and Atoms*, **58**, 85–97,
1108 https://doi.org/10.1016/0168-583X(91)95681-3.

1109 Riu, L., Carter, J. and Poulet, F. 2022. The M3 project: 3 – Global abundance distribution of hydrated
1110 silicates at Mars. *Icarus*, **374**, 114809, https://doi.org/10.1016/j.icarus.2021.114809.

1111 Rivera-Hernández, F., Sumner, D.Y., et al. 2019. Using ChemCam LIBS data to constrain grain size in
1112 rocks on Mars: Proof of concept and application to rocks at Yellowknife Bay and Pahrump Hills,
1113 Gale crater. *Icarus*, **321**, 82–98, https://doi.org/10.1016/j.icarus.2018.10.023.

1114 Röling, W.F.M., Aerts, J.W., Patty, C.H.L., ten Kate, I.L., Ehrenfreund, P. and Direito, S.O.L. 2015. The
1115 Significance of Microbe-Mineral-Biomarker Interactions in the Detection of Life on Mars and
1116 Beyond. *Astrobiology*, **15**, 492–507, https://doi.org/10.1089/ast.2014.1276.

1117 Ross, G.J. and Kodama, H. 1973. Experimental transformation of a chlorite into a vermiculite: Clays.
1118 *Clay Minerals*, 205–211.

1119 Rull, F., Maurice, S., et al. 2017. The Raman Laser Spectrometer for the ExoMars Rover Mission to
1120 Mars. *Astrobiology*, **17**, 627–654, https://doi.org/10.1089/ast.2016.1567.

1121 Salvatore, M.R., Goudge, T.A., et al. 2018. Bulk mineralogy of the NE Syrtis and Jezero crater regions
1122 of Mars derived through thermal infrared spectral analyses. *Icarus*, **301**, 76–96,
1123 https://doi.org/10.1016/j.icarus.2017.09.019.

1124 Schieber, J. 2018. How Small is It? Pushing MAHLI to the Limit in the Search for Mudstones at Gale
1125 Crater, Mars. 1100.

1126 Schopf, J., Farmer, J., Foster, I., Kudryavtsev, A., Gallardo, V. and Espinoza, C. 2012. Gypsum-
1127 Permineralized Microfossils and Their Relevance to the Search for Life on Mars. *Astrobiology*,
1128 **12**, 619–633, https://doi.org/10.1089/ast.2012.0827.

1129 Schuerger, A.C., Golden, D.C. and Ming, D.W. 2012. Biotoxicity of Mars soils: 1. Dry deposition of
1130 analog soils on microbial colonies and survival under Martian conditions. *Planetary and Space*
1131 *Science*, **72**, 91–101, https://doi.org/10.1016/j.pss.2012.07.026.

1132 Simoneit, B.R.T. 2004. Biomarkers (molecular fossils) as geochemical indicators of life. *Advances in*
1133 *Space Research*, **33**, 1255–1261, https://doi.org/10.1016/j.asr.2003.04.045.

1134 Steininger, H., Goesmann, F. and Goetz, W. 2012. Influence of magnesium perchlorate on the pyrolysis
1135 of organic compounds in Mars analogue soils. *Planetary and Space Science*, **71**, 9–17,
1136 https://doi.org/10.1016/j.pss.2012.06.015.

1137 Stevens, A.H., Steer, E., McDonald, A., Amador, E.S. and Cockell, C.S. 2018. Y-Mars: An Astrobiological
1138 Analogue of Martian Mudstone. *Earth and Space Science*, **5**, 163–174,
1139 https://doi.org/10.1002/2017EA000318.

1140 Swayze, G.A., Lowers, H.A., et al. 2018. Characterizing the source of potentially asbestos-bearing
1141 commercial vermiculite insulation using in situ IR spectroscopy. *American Mineralogist*, **103**,
1142 517–549, https://doi.org/10.2138/am-2018-6022.

1143 Tan, J. and Sephton, M.A. 2020. Organic Records of Early Life on Mars: The Role of Iron, Burial, and
1144 Kinetics on Preservation. *Astrobiology*, **20**, 53–72, https://doi.org/10.1089/ast.2019.2046.

1145 Taylor, G.J., Martel, L.M.V., Karunatillake, S., Gasnault, O. and Boynton, W.V. 2010. Mapping Mars
1146 geochemically. *Geology*, **38**, 183–186, https://doi.org/10.1130/G30470.1.

1147 Treiman, A.H., Morris, R.V., et al. 2014. Ferrian saponite from the Santa Monica Mountains (California,
1148 U.S.A., Earth): Characterization as an analog for clay minerals on Mars with application to
1149 Yellowknife Bay in Gale Crater. *American Mineralogist*, **99**, 2234–2250,
1150 https://doi.org/10.2138/am-2014-4763.

1151 Turner, S.M.R. and Bridges, J.C. n.d. Mineralogical Analysis of ExoMars Rover Landing Sites using
1152 CRISM. 1.

1153 Turner, S.M.R., Fawdon, P. and Davis, J.M. n.d. 1 Constraining the Source of Minerals at Oxia Planum,
1154 Mars: Insights into fluvial 2 processes. 27.

1155 Vago, J.L., Westall, F., et al. 2017. Habitability on Early Mars and the Search for Biosignatures with the
1156 ExoMars Rover. *Astrobiology*, **17**, 471–510, https://doi.org/10.1089/ast.2016.1533.

1157 Vaniman, D.T., Bish, D.L., et al. 2014. Mineralogy of a Mudstone at Yellowknife Bay, Gale Crater, Mars.
1158 *Science*, **343**, 1243480–1243480, https://doi.org/10.1126/science.1243480.

1159 Wang, A., Haskin, L.A., et al. 2006. Sulfate deposition in subsurface regolith in Gusev crater, Mars.
1160 *Journal of Geophysical Research: Planets*, **111**, https://doi.org/10.1029/2005JE002513.

1161 Wang, A., Freeman, J.J. and Jolliff, B.L. 2015. Understanding the Raman spectral features of
1162 phyllosilicates. *Journal of Raman Spectroscopy*, **46**, 829–845,
1163 https://doi.org/10.1002/jrs.4680.

1164 Wray, J.J., Ehlmann, B.L., Squyres, S.W., Mustard, J.F. and Kirk, R.L. 2008. Compositional stratigraphy
1165 of clay-bearing layered deposits at Mawrth Vallis, Mars: STRATIGRAPHY OF CLAY-BEARING
1166 DEPOSITS ON MARS. *Geophysical Research Letters*, **35**, n/a-n/a,
1167 https://doi.org/10.1029/2008GL034385.

1168 Yen, A.S., et al. 2005. An integrated view of the chemistry and mineralogy of martian soils. *Nature*,
1169 **436**, 49-54, http://dx.doi.org/10.1038/nature03637.